Coherent backscatter enhancement in bistatic Ku-/X-band radar observations of dry snow

Marcel Stefko[1,*], Silvan Leinss[1,2,*], Othmar Frey[1,3], and Irena Hajnsek[1,4]

[1]ETH Zurich, Institute of Environmental Engineering, 8093 Zurich, Switzerland
[2]Université Savoie Mont Blanc, LISTIC, 74000 Annecy, France
[3]Gamma Remote Sensing, 3073 Gümligen, Switzerland
[4]German Aerospace Center, Microwaves and Radar Institute, 82234 Wessling, Germany
[*]These authors contributed equally to this work.

Correspondence: Marcel Stefko (stefko@ifu.baug.ethz.ch) and Silvan Leinss (silvan.leinss@univ-smb.fr)

Abstract. The coherent backscatter opposition effect (CBOE) enhances the backscatter intensity of electromagnetic waves by up to a factor of two in a very narrow cone around the direct return direction when multiple scattering occurs in a weakly absorbing, disordered medium. So far, this effect has not been investigated in terrestrial snow in the microwave spectrum. It has also received little attention in scattering models. We present the first characterization of the CBOE in dry snow using ground-based and space-borne bistatic radar systems. For a seasonal snow pack in Ku-band (17.2 GHz), we found backscatter enhancement of 50–60% (+1.8–2.0 dB) at zero bistatic angle and a peak half-width-at-half-maximum (HWHM) of $0.25°$. In X-band (9.65 GHz), we found backscatter enhancement of at least 35% (+1.3 dB) and an estimated HWHM of $0.12°$ in the accumulation areas of glaciers in the Jungfrau-Aletsch region, Switzerland. Sampling of the peak shape at different bistatic angles allows estimating the scattering and absorption mean free paths, Λ_T and Λ_A. In the VV polarization, we obtained $\Lambda_T = 0.4 \pm 0.1\,\mathrm{m}$ and $\Lambda_A = 19 \pm 12\,\mathrm{m}$ at Ku-band, and $\Lambda_T = 2.1 \pm 0.4\,\mathrm{m}, \Lambda_A = 21.8 \pm 2.7\,\mathrm{m}$ at X-band. The HH polarization yielded similar results. The observed backscatter enhancement is thus significant enough to require consideration in backscatter models describing monostatic and bistatic radar experiments. Enhanced backscattering beyond the Earth, on the surface of solar system bodies, has been interpreted as being caused by the presence of water ice. In agreement with this interpretation, our results confirm the presence of the CBOE at X- and Ku-band frequencies in terrestrial snow.

1 Introduction

The scattering of electromagnetic waves in any type of medium can be used to characterize some of its structural properties. In radar remote sensing, the scattering characteristics of snow have been intensely studied to derive properties of the snowpack. However, an important effect, the coherent backscatter opposition effect (CBOE), can enhance the radar backscatter return by up to a factor of two. This effect has rarely been considered in descriptions of the backscatter return from snow in monostatic radar experiments (where the transmitter and the receiver are co-located), because even though the CBOE is present, its magnitude cannot be quantified without a bistatic reference measurement (where the transmitter and the receiver are at separate locations). To fully characterize the CBOE, bistatic radar experiments need to be performed.

1.1 Opposition effects in random media

An opposition effect (also referred to as "opposition peak", "opposition surge", "enhanced backscattering", "hot spot", and similar) is any phenomenon in which electromagnetic (EM) radiation scattered from a particular medium exhibits an increase in intensity in the direct return direction and its vicinity. Opposition effects occur at a variety of wavelengths and scattering media, and are caused by a variety of underlying physical phenomena (Hapke, 2012).

The coherent backscatter opposition effect (CBOE), also referred to as coherent backscatter enhancement or weak localization of electromagnetic radiation, occurs when coherent EM radiation is scattered two or more times within a weakly absorbing, disordered medium. In the direct return direction, where wave vectors of the incident and scattered wave are parallel, the EM waves, travelling through the medium along each possible scattering path, can interfere constructively with their time-reversed counterparts (Akkermans et al., 1988; Aegerter and Maret, 2009; Hapke, 2012). This constructive interference enhances the backscatter intensity within a very narrow cone of about 0.01–1 degree width by up to a factor of two, whereas transmission is reduced. In all other directions, scattered waves sum up incoherently and form the incoherent background scatter signal. The angular half-width at half-maximum (HWHM) of the CBOE peak is proportional to the ratio of the wavelength λ and the scattering mean free path Λ_T (Hapke, 2012, Eq. 9.42). The peak tip can be very sharp when high orders of scattering contribute. The peak becomes rounder and less intense when absorption and finite sample thickness limit the contribution of multiple scattering events (Akkermans et al. (1988, Fig. 7), Van Der Mark et al. (1988, Fig. 20)).

The CBOE can occur together with the shadow hiding opposition effect (SHOE). However, the SHOE requires particles to be large enough to cast sharp shadows within a porous medium (fine dust, vegetation canopy). Particles can then hide their own shadow in the direct return direction (Hapke, 1986; Hapke et al., 1996). In contrast to the CBOE, the SHOE is caused by single scattering events while multiple scattering weakens the SHOE effect; absorption is not critical. The HWHM of the SHOE peak is given by the ratio of particle radius and particle-to-shadow distance or extinction length in the medium (Hapke, 2012, Eq. 9.24). For the surface of the Moon, acting as a prototype for virtually all solar system objects with exposed surfaces, both the CBOE and the SHOE contribute with similar parts to the scattered light in the visible light spectrum in the direct return direction (Hapke et al., 1998).

1.2 Observations of the CBOE

Most quantitative measurements of the CBOE that characterize the whole angular width of the peak have been carried out at visible-light wavelengths through laboratory experiments which are easier to realize than radio-frequency field- and planetary experiments (Montgomery and Kohl, 1980; Hapke, 1986; Wolf and Maret, 1985; Akkermans et al., 1986; Wolf et al., 1988; Van Albada et al., 1990; Hapke et al., 1996; Van Albada and Lagendijk, 1985; Kuga and Ishimaru, 1984; Van Albada et al., 1988; Mishchenko et al., 2000). In the context of the Earth's cryosphere, Kaasalainen et al. (2006) investigated and confirmed the presence of 10–60% backscatter enhancement in snow at optical wavelengths (632.8 nm) and interpreted the observed narrow angular peak width (HWHM) of 0.1–1 degree as dominated by the CBOE.

55   In the radio-frequency spectrum, the CBOE is mostly discussed in connection with snow and ice deposits where microwave absorption is relatively weak (Warren and Brandt, 2008; Mätzler and Wegmüller, 1987a, b). In planetary science, it has been proposed as an explanation for the unusually high radar cross-sections of surfaces of various solar system bodies (Muhleman et al., 1991; Black et al., 2001; Hapke et al., 1993). It has also been discussed as a potential cause of the unusual radar echoes from the Greenland ice sheet (Rignot et al., 1993), although internal reflections were proposed as an alternative explanation

60   (Rignot, 1995). In both of these contexts, additional measurements at small but nonzero bistatic angles were desired (but not feasible), as they would have provided a way to more easily and robustly characterize the effect (Hapke, 1990; Rignot, 1995). Bistatic radar measurements of surfaces of solar system bodies are possible by using an orbiting spacecraft in combination with the deep space network receivers on Earth (Simpson, 1993; Palmer et al., 2017). However, such experiments require a very specific geometric alignment of the spacecraft's orbit with respect to the Earth and are thus not common. Nevertheless, several

65   experiments were carried out with the Moon as the target (Yushkova et al., 2018): the Clementine bistatic radar experiment observed an opposition peak in certain areas of the lunar surface. This peak has been suggested to be attributable to the CBOE which implied the existence of ice deposits on the surface (Nozette et al., 1996), though other work has called the interpretation of the Clementine data into question (Simpson and Tyler, 1999). More recently, the Mini-RF instrument of the Lunar Reconnaissance Orbiter, in concert with the Arecibo Observatory's radio telescope acting as transmitter, detected the

70   opposition surge in certain areas of the lunar surface, again attributed to the presence of near-surface deposits of water ice (Patterson et al., 2017).

In many of these experiments, observation of a backscatter enhancement peak at radio-frequencies has been interpreted as the CBOE and has been used to infer the possible existence of water ice on the surface of the corresponding solar system bodies. Other works considered the CBOE in microwave scattering models of terrestrial snow (Tan et al., 2015) but could not

75   analyze the peak shape of the CBOE. In this work we demonstrate that the existence of snow on the Earth can indeed cause a CBOE. We present a sampling of the peak shape at Ku- and X-band radio wavelengths with ground-based and space-borne imaging radars.

2   Methods

To characterize the angular peak of backscatter enhancement effects in the radio-frequency spectrum, we used two bistatic

80   radar systems, the ground-based system KAPRI and the space-borne satellite formation TanDEM-X. For both systems, the transmitter and receiver are placed on independent platforms and thus the bistatic angle can be varied. The bistatic angle β is defined as the angle between the transmitter, the observed location, and the bistatic receiver. In the exact direct return direction, the bistatic angle is zero and the scattering alignment is called the monostatic configuration.

2.1   Ground-based observations - KAPRI

85   KAPRI (Baffelli et al., 2017) is a ground-based Ku-band FMCW real-aperture radar system developed by Gamma Remote Sensing, capable of performing fully-polarimetric bistatic measurements. In the bistatic configuration comprised of two KAPRI
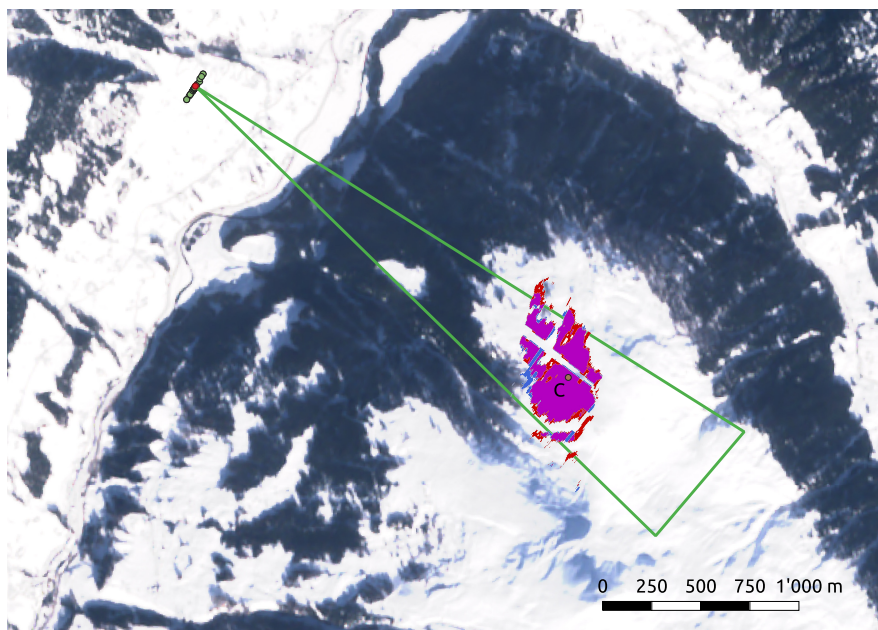
Figure 1. Map of the ground-based bistatic radar experiment. The position of the fixed transmitter (red dot) and the different receiver positions (green dots) are marked in upper left corner. The green triangle marks the $-3\,\mathrm{dB}$ antenna beamwidth of $12°$ of the receiver device. The antennas are oriented towards the snow covered north-west face of the mountain Rinerhorn, Switzerland. The region of interest (ROI) for the winter and summer seasons is shown in blue and red respectively. Their overlap is shown in purple. C is a reference point for the orientation of the bistatic receiver (see Fig. 4). The hollow line slicing through the ROI masks out metallic beams from a ski-lift on the slope. Satellite imagery data: Sentinel-2 on 20 February 2021. Modified Copernicus Sentinel data 2021/Sentinel Hub.

devices with different antenna configurations (Stefko et al., 2021b), it offers coverage of areas hundreds of meters wide at a range of several kilometers. It operates at central frequency $17.2\,\mathrm{GHz}$ ($\lambda = 1.74\,\mathrm{cm}$), with $200\,\mathrm{MHz}$ bandwidth. The system and the processing pipeline for bistatic KAPRI datasets are described in detail in (Stefko et al., 2021b). Details of the antenna

90   configuration while using a cable synchronization setup can be found in (Stefko et al., 2021a, Fig. 2).

2.1.1 Observation site: Rinerhorn, Davos

For the ground-based experiment (map shown in Fig. 1), the observed region of interest (ROI) was located on the north-western face of Rinerhorn peak near Davos, Switzerland. Both devices were located on the valley side opposite the peak, at 46.763 N, 9.788 E (Fig. 1). The radar location features a straight and relatively flat segment of road approximately $200\,\mathrm{m}$

95   long with unobstructed view of Rinerhorn. The devices were placed at approximately $1620\,\mathrm{m}$ altitude, while the ROI altitude spans from $2050\,\mathrm{m}$ to $2270\,\mathrm{m}$. With this upward-looking observation geometry the vast majority of the ROI area is observed under a shallow local incidence angle larger than $70°$. Problems with multipath interference arising from the upward-looking
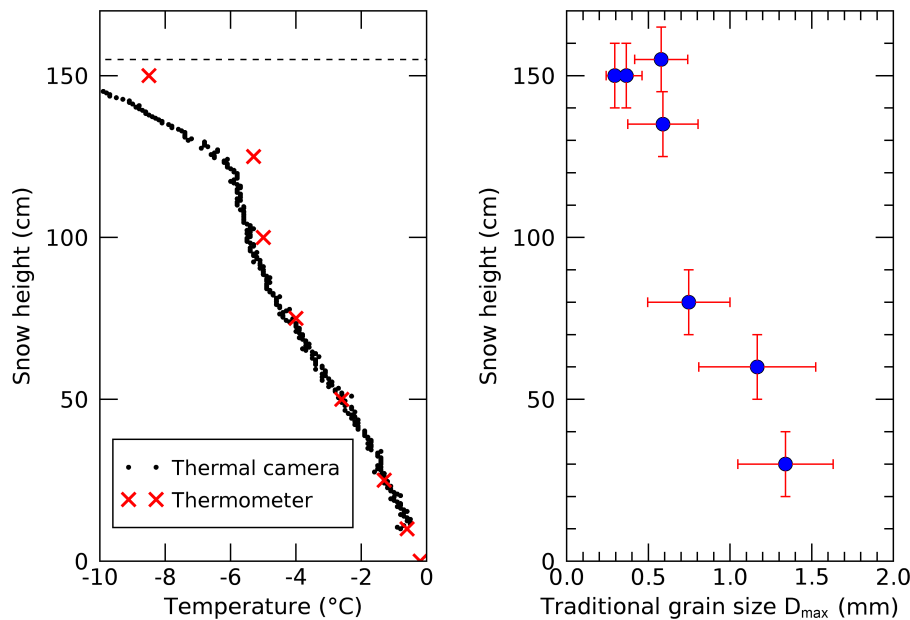
Figure 2. Snow temperature and grain size in the study area close to point C in Fig. 1 on 18 February 2021. Snow height is 1.55 m.

observation geometry while employing a fan-beam radar system (Lucas et al., 2017) are avoided by placing the instruments on the opposing side of the valley.

100 We performed two experiments: in summer (05 August 2020), the ROI was covered by low grass. In winter (18 February 2021), the area was completely covered by approximately 1.5 m of seasonal snow. Each measurement began at approximately 08:00 local time, and the total duration of the observations was 3.5 hours in summer, and 5.5 hours in winter. In winter, a snow pit revealed snow temperatures of $-10\,°\text{C}$ at the snow surface and $-0.2\,°\text{C}$ at the bottom of the snowpack (Fig. 2, left). The classical snow grain size, measured as the mean maximum extent of snow crystals (Fierz et al., 2009), was $D_{\text{max}} = 0.3\,\text{mm}$ at
105 the surface and $1.5\,\text{mm}$ at the base (Fig. 2, right).

  To select the ROI, a mask fulfilling the following three conditions was applied for each season: 1) Include only terrain higher than the tree line at $2050\,\text{m}$ altitude. 2) Exclude areas containing man-made structures (metallic support beams, metal ropes, buildings, corner reflectors). 3) Exclude areas affected by radar shadow and exclude areas outside of the main beam of the secondary antennas – these areas were detected by applying a threshold on the magnitude of the single-pass interferometric
110 coherence γ of the secondary receiver in the VV channel. In every acquisition in the summer dataset, pixels with $\gamma < 0.85$ were masked out, in the winter dataset pixels with $\gamma < 0.80$ were masked out. A sliding window of 5×3 (range $\times$ azimuth) pixels was used for coherence estimation. The winter threshold is lower due to lower overall coherence as opposed to summer.

  The masks defining the ROI for each season are shown in Fig. 1. They cover practically the same region of the hillside. The acquired calibrated SLC datasets were spatially multi-looked using a 5×3 window to obtain the intensity images, and analyzed
115 in the radar polar geometry (range$\times$azimuth angle). The intensity value $\hat{I}(\beta)$ (the hat symbol $\hat{}$ indicates it's a measured quantity)

was computed for every acquisition by averaging the measured intensities of all pixels within the ROI. We analyzed only the VV and HH polarization as the cross-polarized signal was too close to the noise floor to provide reliable data.

2.1.2 Device configuration and measurement procedure

The primary (monostatic) transmitter-receiver remained stationary during the experiment (Fig. 3, top) and performed azimuthal
120 sweep acquisitions of the observed area at a range of approximately 2.5 km. The secondary device (bistatic receiver) was moved step-wise to sample bistatic angles between 0.04° and 1.92°. In winter, the secondary device was mounted on a large sledge (Hornschlitten, Fig. 3, middle). In summer, a wheeled cart was used as a movable radar platform (Fig. 3, bottom). The trajectory of the secondary device is visualized in Fig. 4.

The bistatic angle β was calculated for each position of the secondary receiver S as

125
$$\beta = \arctan \frac{b}{d_{\mathrm{PC}}}. \tag{1}$$

The length of the bistatic baseline b is given by the length of the vector between the primary and secondary radar's positions, after projecting it into the plane orthogonal to the line of sight. The line of sight is the vector between the primary radar P and the reference point C in the ROI (see Fig. 4). Its length is $d_{\mathrm{PC}} = 2500\,\mathrm{m}$.

To ensure optimal overlap of the antenna patterns in the ROI, the secondary device was leveled and oriented manually in
130 each position. The pitch and roll angles of the mobile platform with respect to the true vertical direction were measured with a digital spirit level at each measurement point, and did not exceed 2° in either direction. In azimuth, the device was oriented with a compass and optical viewfinder using a reference point in the center of the ROI (Point C in Fig. 1). The estimated precision is 1°.

The transmit antennas on the primary KAPRI device have a physical horizontal length of 2 m (Fig. 3, top), and thus the
135 bistatic angle at 2.5 km range differs by $\sim 0.05°$ between the two edges of the transmit antenna. This imposes a practical limit on the resolution of the sampling of the intensity curve: any variation of intensity within bistatic angles of less than 0.05° will be smeared out by the non-zero size of the transmit antennas.

2.1.3 KAPRI: radiometric precision

Three main factors were identified which can affect the radiometric precision of the measurements: temporal drift of the
140 scattering properties in the ROI, the radiometric stability of the bistatic KAPRI system, and the pointing precision of the secondary receiver's antennas.

The trajectory of the bistatic receiver (Fig. 4) was designed to repeatedly increase and decrease the absolute value of the bistatic baseline. This allows detection of any temporal drift of the scattering intensity over the course of the measurement (i.e. on the order of minutes to hours). Drifts would be detected by the different shape of the left and right wing of the intensity
145 curve $\hat{I}(\beta)$.

Figure 3. Top: primary KAPRI radar tower (monostatic device) during the ground-based experiment equipped with narrow-beam traveling-wave antennas. Center: secondary KAPRI radar tower (bistatic receiver) equipped with horn antennas and deployed on a "Hornschlitten" sledge in winter. Bottom: secondary KAPRI tower deployed on a wheeled cart in summer.
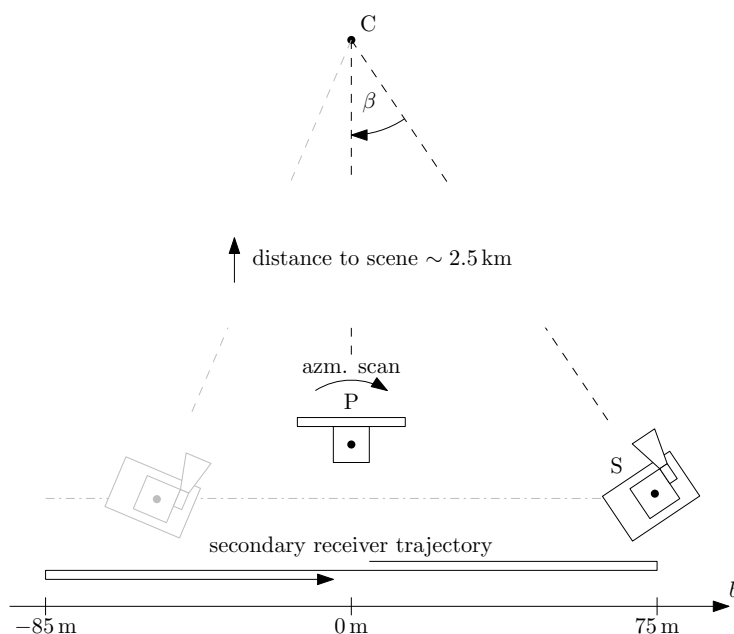
Figure 4. Diagram of the ground-based measurement procedure. The stationary, primary device P performs repeated azimuthal scans of the ROI around point C. To sample the scattering response of the ROI under a variety of bistatic angles β, the mobile secondary device S is repositioned in-between acquisitions. For both winter and summer experiments, S was placed at bistatic baselines b varying between -85 and $+75$ m relative to P.

The radiometric stability of KAPRI can be assessed by investigating the monostatic scattering intensity observed by the monostatic device from a reference target (a corner reflector). The maximal detected variation was observed in the HH channel in the winter season, with standard deviation of 16% relative to the mean value.

For each individual measurement the beam pointing direction of the secondary receiver differed by less than $1°$ in azimuth from the ideal central pointing direction towards point C. Due to the antenna pattern of the secondary receiver (Stefko et al., 2021b, Fig. 7), an azimuthal misalignment of $1°$ can reduce the signal intensity by not more than ~ 1 dB (25%) at the edge of the "ideal" antenna pattern footprint covering the ROI. However, when considering the total received backscatter from the ROI, this reduction is partially compensated, since the observed backscatter intensity from the other edge of the ROI would necessarily increase.

Due to the limited radiometric stability and the beam pointing uncertainty the observed backscatter intensity can thus be expected to vary stochastically with estimated standard deviation of approximately 20%, affecting each individual measurement by a significant amount. These effects are difficult to compensate for, since there were no reference targets in the scene with a sufficiently high and stable bistatic radar cross-section. For this reason, no a-posteriori radiometric calibration was applied to the data. However, the two effects are stochastic in nature, and uncorrelated between individual receiver positions, and thus
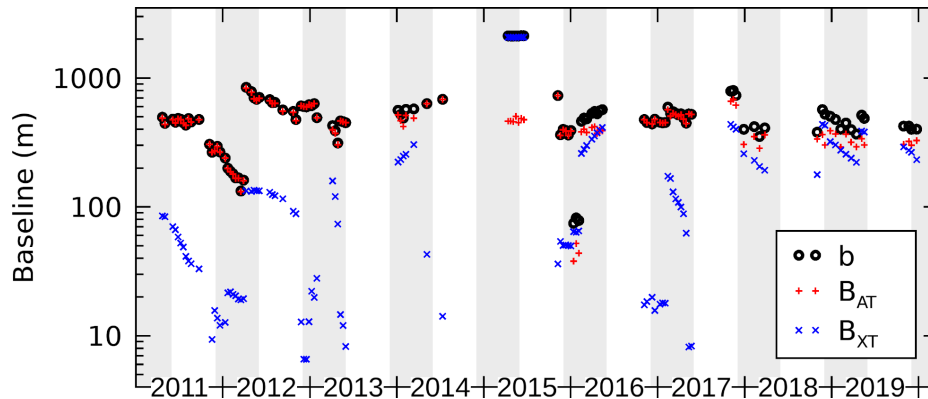
Figure 5. Time series of the bistatic baselines b according to Eq. (2) together with along- and across-track baselines B_{AT} and B_{XT} of the TanDEM-X satellite acquisitions of the Jungfrau-Aletsch region. Along-track baselines are adjusted by $30\,\mathrm{m}$ due to the satellite motion (see Sect. 2.2.3). Gray shading indicates the period from 1 December until 31 May for which we assume that the firn, present in the accumulation area $> 3500\,\mathrm{m}$, is completely frozen.

160   with a sufficiently high number of acquisitions, the enhancement peak should still be detectable, albeit with lower radiometric precision.

2.2   Satellite observations - TanDEM-X

The TanDEM-X satellite formation is the first space-borne bistatic radar system with an adjustable bistatic baseline. The formation consists of two free flying synthetic aperture radar (SAR) satellites, TerraSAR-X and TanDEM-X, orbiting the Earth

165   in about 514 km height in a helix-like formation (Krieger et al., 2007). The two radar instruments operate at X-band at a central frequency of $9.65\,\mathrm{GHz}$ ($\lambda = 3.11\,\mathrm{cm}$). Depending on the acquisition mode, both satellites can act as either transmitter or receiver or both. In the bistatic mode, the transmit-receive satellite operates in a monostatic observation geometry, and the receive-only satellite operates in a bistatic observation geometry.

Since the launch of TanDEM-X in June 2010, the distance between the two satellites has been varied by several kilometers.

170   The largest (and smallest) distances were obtained during the TanDEM-X science phase between Oct 2014 and February 2016 (Hajnsek et al., 2014). To find an area best suited for observation of the CBOE in X-band, we searched the entire TanDEM-X archive for areas that are covered by deep snow and where long acquisition time series with large bistatic angles are available. Unfortunately, near the poles, bistatic angles are relatively small, making a sufficient sampling of the CBOE peak difficult. At the equator, the largest bistatic angles of up to $0.35°$ are available but snow is naturally rare. As a best compromise, we selected

175   the Jungfrau-Aletsch region in Switzerland and the Teram-Shehr/Rimo glacier in the Karakorum.

2.2.1 Primary observation site: Jungfrau-Aletsch region

The Jungfrau-Aletsch region has been selected as a TanDEM-X super test site with the aim to acquire as many acquisitions as possible, and to explore the scientific value of the bistatic radar mission. 118 bistatic acquisitions in the two polarizations (VV, HH) were acquired between 2011 and 2019, most of them during winter (Fig. 5). For 104 acquisitions, TerraSAR-X acted as transmitter, for 14 TanDEM-X. Bistatic baselines between 65 and 2100 m are available, corresponding to $\beta = 0.005 - 0.21°$. The incidence angle at the scene center is $\theta = 32°$ (orbit 154, descending). Time-averaged backscatter images of the study area are provided in the supplementary figures S2 and S3. Interferometric and polarimetric properties of the dataset were analyzed by Leinss and Bernhard (2021).

The Jungfrau-Aletsch region is highly glaciated with multiple peaks reaching above 4000 m. Cold firn, several tens of meters deep, is likely present throughout the year: depending on exposition, the transition to temperate firn is at 3400–4000 m while the upper 15 m of firn experience seasonal temperature cycles and can freeze in winter (Suter et al., 2001; Suter and Hoelzle, 2002; Jun et al., 2002). In March 2021, firn temperatures of $-11 \pm 3°C$ in the upper two meters, and $-4 \pm 2°C$ at -8 m, were measured by Bannwart (2021) at two sites, one on 3380 m (46.5525°N / 8.0286°E) and on 3350 m (46.5483°N / 8.0323°E). The region contains Great Aletsch Glacier (46.50°N, 8.03°E), the largest glacier in the European Alps. Its equilibrium line altitude, above which accumulation dominates, is at ~3000m (Zemp et al., 2007). In the ablation area below, seasonal snow is present. Ice free areas are dominated by rock and scree. Below 2500 m vegetation dominates with a tree line of 2000 m. For analysis of specific land cover types, we selected the following three regions of interest (ROI) in the Jungfrau-Aletsch region (shown also in the supplementary figure S8):

1. The accumulation area of glaciers with altitudes above 3500 m. These areas are at or above the temperate-to-cold firn transition and we assume that firn conditions did not change too drastically from winter to winter. To ensure refreezing of firn after summer, and to avoid snow melt in spring, we restricted the model parameter estimation on data acquired between 01 December and 31 May (gray shading in Fig. 5). The dry, deep firn acts as a thick medium with multiple scattering in the volume but low absorbing.

2. The ablation area of Great Aletsch Glacier with altitudes below 2700 m. Field measurements indicate a seasonal snow cover of 0–3 m on the glacier tongue during winter (Leinss and Bernhard, 2021). The seasonal snow acts as a thin medium of volume scatterers with low absorption.

3. Forested areas with at least 7 m height, mainly conifer forest located in the Rhone valley and the Grindelwald region. The Forest acts as a medium where volume scattering can occur but absorption is strong.

2.2.2 Secondary observation site: Teram-Shehr/Rimo Glacier

On the plateau beetween Teram-Shehr and Rimo Glacier (35.47°N, 77.30°E), we selected the accumulation area above 6100 m. The equilibrium line altitude of Teram-Shehr glacier, an eastern tributary of Siachen glacier in the Karakorum, is at approximately 5250 m (Agarwal et al., 2017). Compared to the Jungfrau-Aletsch dataset, considerably fewer acquisitions are available

here and bistatic angles are not significantly larger: for orbit 98 ($\beta = 0.04$–$0.23°$, $\theta = 39°$, asc.) nine acquisitions showed dry firn and 17 acquisitions wet or partially wet firn. For orbit 75 ($\beta = 0.04$–$0.19°$, $\theta = 43°$, desc.) we found 18 acquisitions with

210   dry firn and 25 with wet firn. Both datasets contain the HH polarization only. To ensure refreezing of firn after summer, we restricted the analysis to data between 01 December and 30 June.

2.2.3   TanDEM-X: bistatic angle

For TanDEM-X, the bistatic angle $\beta = b/R$ was determined from the average slant-range distance R to the scene center and from the bistatic baseline b, derived from the orbit coordinates. To compute b, the distance between the two satellites was

215   decomposed into the along-track baseline B_{AT}, the across-track baseline B_{XT} and the parallel, or line-of-sight baseline baseline B_{LOS}. The bistatic baseline b, perpendicular to the line-of-sight direction, is given by

$$b = \sqrt{B_{\mathrm{AT}}^2 + B_{\mathrm{XT}}^2}. \tag{2}$$

Figure 5 shows time series of b, B_{AT}, and B_{XT}. Because of the bistatic acquisition geometry, where the phase center of the bistatic receiver is located in the midpoint between the transmitter and the receiver (Duque et al., 2012), the across and along-

220   track baselines used in Eq. (2) are a factor of two larger than the effective interferometric across- and along-track baselines given in the acquisition's meta-information (Leinss and Bernhard, 2021, cf. Fig. 2).

Even though we refer in the following to the monostatic acquisition, we note, that the orbital velocity of $v = 7.6\,\mathrm{km\,s^{-1}}$ results in a small, velocity induced, bistatic angle of $\beta_v = 0.003°$ for the monostatic receiver, because the satellite moves 30 m between transmission and reception of a radar pulse. The high orbital velocity also decreases (increases) the along-track

225   baseline B_{AT} by 30 m when the bistatic receiver follows (is ahead of) the transmitter. We considered this in the analysis but found the effect negligible.

2.2.4   TanDEM-X: radiometric calibration and computation of backscatter ratios

Resolving the peak shape of the CBOE with a maximum expected peak height of 3 dB requires a precise radiometric calibration of the bistatic dataset. To avoid any terrain or incidence angle dependent calibration, we analyzed the ratio between

230   the backscatter intensity $\hat{I}_{\mathrm{bist}}$ observed by the bistatic receiver and the intensity $\hat{I}_{\mathrm{mono}}$ observed by the monostatic transmitter-receiver:

$$\hat{I}_{\mathrm{r},0} = \hat{I}_{\mathrm{bist}}/\hat{I}_{\mathrm{mono}}. \tag{3}$$

The index r,0 indicates taking the ratio relative to $I(\beta = 0)$. Averaging ratios like $\hat{I}_{\mathrm{r},0}$ would result in a biased estimate. To estimate unbiased spatially or temporally averaged ratios we first applied the averages on $\hat{I}_{\mathrm{bist}}$ and $\hat{I}_{\mathrm{mono}}$ and then computed the

235   ratio $\hat{I}_{\mathrm{r},0}$. We use $\hat{I}$ to refer to the radar brightness commonly denoted by β_0 (Raney et al., 1994) to avoid confusion with the bistatic angle β. The hat symbol ˆ indicates measured quantities.

For every orbit and each polarization channel, we coregistered time series of the interferometric TanDEM-X CoSSC (Coregistered Single look Slant range Complex) acquisition pairs (Fritz et al., 2012; Duque et al., 2012). To obtain the intensities

$\hat{I}_{\mathrm{mono}}$ and $\hat{I}_{\mathrm{bist}}^{\mathrm{uncal.}}$, we detected the temporally coregistered CoSSCs, applied 10×10 pixels multilooking, and downsampled the

240   data by a factor of 10.

Unlike the monostatic products, the bistatic TanDEM-X products are not radiometrically calibrated (Fritz et al., 2012, Sect. 4.3). The intensity ratio $\hat{I}_{\mathrm{r,0}}^{\mathrm{uncal.}} = \hat{I}_{\mathrm{bist}}^{\mathrm{uncal.}} / \hat{I}_{\mathrm{mono}}$ showed, therefore, differences of 10–30% between the bistatic and the monostatic receiver. While in the VV polarization $\hat{I}_{\mathrm{r,0,VV}}^{\mathrm{uncal.}}$ showed spatially relatively constant values at small bistatic angles, $\hat{I}_{\mathrm{r,0,HH}}^{\mathrm{uncal.}}$ showed terrain-independent trends of a few percent, presumably due to different antenna patterns (supplementary Figs. S4 and S5). To

245   compensate for these patterns, we calibrated for each polarization the intensity $\hat{I}_{\mathrm{bist}}^{\mathrm{uncal.}}$ with the ratio of the pixel-wise temporal mean $\langle \cdot \rangle^{\mathrm{temp.}}$ of 17 scenes with $\beta < 0.033°$. This threshold for β was chosen small enough to avoid any significant bias from backscatter enhancement. The bistatic intensity after antenna calibration is

$$\hat{I}_{\mathrm{bist}}^{\mathrm{ant.cal.}} = \hat{I}_{\mathrm{bist}}^{\mathrm{uncal.}} \frac{\langle \hat{I}_{\mathrm{mono}} \rangle_{\beta < 0.033°}^{\mathrm{temp.}}}{\langle \hat{I}_{\mathrm{bist}}^{\mathrm{uncal.}} \rangle_{\beta < 0.033°}^{\mathrm{temp.}}} \qquad (4)$$

To obtain the calibrated intensity $\hat{I}_{\mathrm{bist}}$, we compensated in each acquisition pair for the remaining spatially constant offset

250   between the monostatic and bistatic data. For this we multiplied $\hat{I}_{\mathrm{bist}}^{\mathrm{ant.cal.}}$ with the ratio of the monostatic and bistatic radar brightness, spatially averaged, as indicated by $\langle \cdot \rangle_{\mathrm{cal.area}}^{\mathrm{spat.}}$, over a pre-defined calibration area:

$$\hat{I}_{\mathrm{bist}} = \hat{I}_{\mathrm{bist}}^{\mathrm{ant.cal.}} \frac{\langle \hat{I}_{\mathrm{mono}} \rangle_{\mathrm{cal.area}}^{\mathrm{spat.}}}{\langle \hat{I}_{\mathrm{bist}}^{\mathrm{ant.cal.}} \rangle_{\mathrm{cal.area}}^{\mathrm{spat.}}} . \qquad (5)$$

For calibration of the Jungfrau-Aletsch dataset we used areas that showed a temporally stable and baseline-independent backscatter ratio $\hat{I}_{\mathrm{r,0}}$. These areas were defined using two iterations. In a first iteration, we masked out very dark areas, possibly

255   affected by noise, such as shadow ($\hat{I}_{\mathrm{mono}} < -14\,\mathrm{dB}$) and also very bright areas such as layover and strong local scatterers ($\hat{I}_{\mathrm{mono}} > +1\,\mathrm{dB}$) through thresholding the temporal mean of the backscatter intensity. We also masked out the ROIs later analyzed, by masking elevations above $3000\,\mathrm{m}$ where multi-year firn occurs, regions covered by forest, as well as the ablation area of Great Aletsch Glacier. After using the remaining pixels for calibration, in the second iteration we masked out additionally areas where $\hat{I}_{\mathrm{r,0}}$, computed pixel-wise using the temporal means of $\hat{I}_{\mathrm{mono}}$ and $\hat{I}_{\mathrm{bist}}$ from 43 acquisitions with bistatic angles

260   smaller than $0.04°$ (cf. Eq. (4)), differed more than 5% from unity. Such deviations appeared in areas of low radar backscatter and areas not directly affected by layover but next to layover in the far-range direction. The deviations might originate from bright azimuth or range-ambiguities or areas affected by sidelobes of layover (also visible in supplementary figures S4 and S5). We also removed areas where the pre-calibrated backscatter ratio $\hat{I}_{\mathrm{r,0}}$ showed a temporal standard deviation larger than 0.08 (supplementary figures S6 and S7). Finally, to avoid that the CBOE or possibly the SHOE affect the calibration, we masked out

265   areas that showed more than 5% enhanced scattering in the direct return direction in the large-baseline acquisitions $B_\perp > 2\,\mathrm{km}$. In total, we masked out approximately 50% of pixels from the scene (supplementary Fig. S8) and used the remaining pixels, mainly grassland, rock and the ablation areas of glaciers for calibration in Eq. (5). In this data-driven calibration we assume that the regions selected for calibration show an equal backscatter intensity for the monostatic and bistatic receiver.

The Teram-Shehr dataset did not provide enough suitable acquisitions for antenna calibration according to Eq. (4). For

270   calibration with Eq. (5), we used the glacier tongue (ablation area, below $5000\,\mathrm{m}$).

To determine the backscatter ratio for the ROIs (see Sect. 2.2.1 and Sect. 2.2.2), we used Eq. (3) with $\hat{I}_{\mathrm{bist}}$ and $\hat{I}_{\mathrm{mono}}$ averaged over the ROI. In addition, the mean backscatter intensity $\hat{I}_{\mathrm{mono}}$ was used as a proxy to differentiate between dry and wet snow for snow covered areas.

To display imagery of $I_{\mathrm{r},0}$ with sufficient radiometric resolution, we applied additional 4×4 px multilooking to the down-
275   sampled backscatter imagery, corresponding to an effective multilooking operation of 41×41 pixels. This value was chosen to keep the standard deviation $\sigma = I/\sqrt{N}$ of the multilooked intensity I sufficiently low (Oliver and Quegan, 2004). N is the number of looks. Given that adjacent pixels are statistically not completely independent (the SLC data is oversampled by a factor of 1.3 in slant range and and 2.9 in azimuth, resulting in 3.73 pixels per look) we obtain a value of $N = 41^2/3.73 = 450$ looks which corresponds to a radiometric accuracy (standard deviation) of $0.2\,\mathrm{dB}$ (5%) at an intensity of $I = -5\,\mathrm{dB}$.

280   ## 2.3   Backscatter model for the CBOE

For interpretation and modeling of our results we considered the book from Hapke (2012). In Chapter 9, Eqs. 9.40 and 9.44, as well in (Akkermans et al., 1986, 1988), the peak shape of the coherent backscatter enhancement is described for non-absorbing or absorbing media with the equation:

$$B_C(\beta) = \frac{1}{[1 + 1.42K][1 + \xi(\beta)]^2} \left[1 + \frac{1 - e^{-1.42K\xi(\beta)}}{\xi(\beta)} \right] \tag{6}$$

285   where $B_C(\beta)$ is the magnitude of the coherent backscatter intensity enhancement at bistatic angle $\beta \approx \sin\beta$ relative to the incoherent background I_0. Depending on absorption, $B_C(0)$ has a height between 0 and 1 and $B_C(\infty) = 0$ (Fig. 6). The background intensity I_0 is determined by the incoherent scattering properties of the medium so that

$$I(\beta) = I_0(1 + B_C(\beta)) \tag{7}$$

describes the total backscatter intensity $I(\beta)$ in the proximity of several degrees from the direct backscatter direction. K is the
290   medium porosity coefficient (see below). For notational simplicity we defined

$$\xi(\beta) = \sqrt{\left(\frac{2\pi\Lambda_T\beta}{\lambda}\right)^2 + \frac{3\Lambda_T}{\Lambda_A}}. \tag{8}$$

In this equation λ is the wavelength in the medium, Λ_T is the transport mean free path, and Λ_A is the absorption mean free path. The length of the transport mean free path Λ_T is a measure of the medium's scattering properties, and corresponds to the scattering mean free path Λ_S for particles that scatter EM radiation isotropically (Hapke, 2012, Eq. 7.24b). Correspondingly,
295   Λ_A is a measure of the medium's absorbing properties. For negligible scattering, Λ_A describes the absorption length where the incident radiation is reduced to $1/e$; a non-absorbing medium would have $\Lambda_A = \infty$. Similar, for negligible absorption, Λ_T describes the one-way penetration depth where the incident radiation has been reduced to $1/e$ by side-way scattering.

The porosity coefficient is $K = 1$ for weakly scattering media in which Λ_T is much longer than the size of scatterers. This follows from Hapke (2012, Eq. 7.44) where the product of the extinction coefficient $E = \Lambda_S^{-1} + \Lambda_A^{-1}$ and the distance between
300   scattering particles L must be $EL \ll 1$. For dry snow at X- and Ku-band wavelengths where the one-way penetration depth
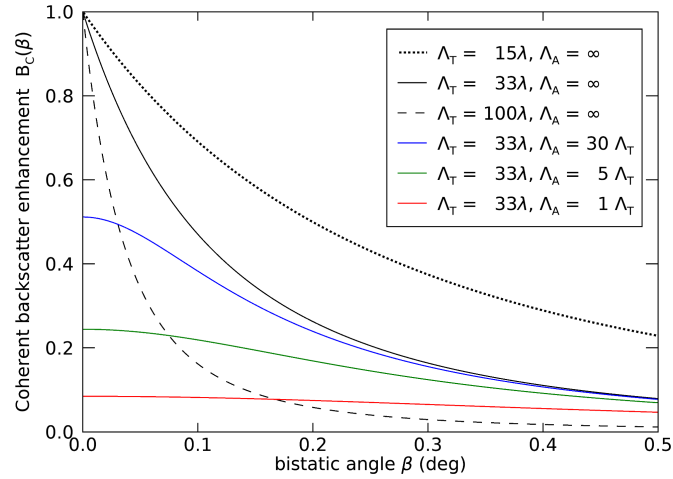
Figure 6. Modeled peak shape of the CBOE for different scattering mean free paths Λ_T given in multiples of the wavelength λ and for different absorption mean free paths Λ_A (in multiples of Λ_T) in a medium with small scattering particles (porosity coefficient $K = 1$). For a non-absorbing medium ($\Lambda_A = \infty$) a very sharp peak can be observed. Already with a weak absorption $\Lambda_A = 30\Lambda_T$ (blue) the peak height is reduced to 50% and the peak becomes much rounder. For comparable scattering and absorption lengths the peak is not noticeable (red).

($\approx \Lambda_S$) is on the order of meters, where absorption is negligible ($\Lambda_A \gg \Lambda_S$), and where the particle (or lattice) distance L can be approximated by the snow grain size r_g (millimeters), we obtain $EL \approx \Lambda_S^{-1} r_g \approx 10^{-3} \ll 1$ which justifies $K = 1$.

The peak shape, as drawn in Figure 6, is determined by the ratio of scattering mean free path Λ_T to the wavelength λ and by the probability distribution of scattering path lengths in the medium. A (monostatic) scattering path begins at the first
305 scattering event in the medium, travels along multiple scatter events with mean distance Λ_T, and ends when the radiation is scattered back out of the medium in the direct return direction (Hapke, 2012, Chapter 9.3). In the monostatic configuration, radiation traveling along such a path interferes constructively with radiation propagating along the time-reversed counterpart, thus causing the backscatter intensity enhancement. Long scattering paths, consisting of multiple scattering events, have a longer distance between the path's start and end point and cause a narrow peak, while short scattering paths cause a broad
310 peak. The final peak shape is determined by the sum of all occurring peak shapes of different widths, weighted according to their occurrence probabilities. The more absorption occurs, the shorter are the scattering paths that can contribute to the coherent peak, and the lower is the probability for the occurrence of higher order scattering, hence the peak becomes rounder (Akkermans et al., 1988, Fig. 7). Long scattering paths can also be suppressed by a finite sample thickness, which also causes a rounding of the peak (Van Der Mark et al., 1988, Fig. 20). Figure 6 shows the shape of the CBOE peak for a range of values of
315 Λ_T, Λ_A given in multiples of λ. Longer scattering lengths Λ_T cause a narrower peak, while the peak height and the curvature near $\beta = 0$ is determined by Λ_A. Hence, when characterizing the full peak shape, Λ_T and Λ_A can be determined.

2.3.1 Application to KAPRI data

With the ground-based KAPRI instrument, the benefit of the flexible configuration allows us to sample the intensity peak up to relatively high value of bistatic angle β, and thus the flat region of the intensity curve ($I(\beta \to \infty) \to I_0$) should be observable.
320 However, the very top of the peak is difficult to sample due to the non-negligible size of the primary device's antennas, as well as the possibility of the devices obstructing each other's view when placed very close together. Because of this, for analysis of KAPRI data, we use the intensity ratio $I_{r,\infty}(\beta)$ which is normalized to the incoherent background intensity $I(\infty)$, and can be expressed with aid of Eq. (7) as:

$$I_{r,\infty}(\beta) = \frac{I(\beta)}{I(\infty)} = \frac{I_0(1 + B_C(\beta))}{I_0(1 + B_C(\infty))} = 1 + B_C(\beta) \tag{9}$$

325   To calculate the intensity ratio of Eq. (9) from the actual observed mean ROI intensity $\hat{I}(\beta)$, we approximate $I(\infty)$ as the mean value of $\hat{I}(\beta)$ from all acquisitions within the corresponding dataset where $\beta > 1°$ (i.e. values well within the flat region of the intensity curve):

$$\hat{I}_{r,\infty}(\beta) \approx \frac{\hat{I}(\beta)}{\langle \hat{I}(\beta) \rangle_{\beta > 1°}} \tag{10}$$

Because the model $B_C = B_C(\beta, \Lambda_T, \Lambda_A)$ depends on the transport mean free path Λ_T and absorption length Λ_A through
330 Eqs. (6) and (8), we can use Eq. (9) to fit different values of Λ_T, Λ_A to the observed intensity curve $\hat{I}_{r,\infty}(\beta)$ by nonlinear least square minimization. For the fitting procedure, we used the TRF (trust region reflective) optimization method implemented via the `curve_fit` function of the `scipy.optimize` library (Virtanen et al., 2020). The initial parameter values of the (Λ_T, Λ_A) pair were set to $(1\,\text{m}, 100\,\text{m})$, and both parameters were restricted to the non-negative real number domain.

2.3.2 Application to TanDEM-X data

335 With TanDEM-X we measured the intensity ratio $\hat{I}_{r,0}(\beta)$ between the bistatic receiver $\hat{I}_{\text{bist}} = \hat{I}(\beta > 0)$ and the monostatic receiver $\hat{I}_{\text{mono}}(\beta_v = 0.003°) \approx I(0)$ (Sect. 2.2.3). This approximation is well justified considering that the expected width of the peak is at least one order of magnitude larger than the small bistatic angle of the monostatic receiver (cf. Fig. 6) and that rounding of the peak tip due to weak absorption can be expected. The TanDEM-X measurement can, therefore, be described by Eq. (7) as:

340 $$I_{r,0}(\beta) = \frac{I(\beta)}{I(0)} = \frac{I_0(1 + B_C(\beta))}{I_0(1 + B_C(0))} = \frac{1 + B_C(\beta)}{1 + B_C(0)} \tag{11}$$

The intensity ratio $I_{r,0}(\beta)$ is 1.0 for $\beta = 0$ and reaches its minimum 0.5 at $\beta \to \infty$ when absorption is negligible. With increasing absorption the contrast lowers and $I_{r,0}(\beta \to \infty)$ increases from 0.5 to eventually 1.0.

A lower limit for the enhancement $B_C(\beta = 0)$ can be quickly estimated: because $B_C(\beta_{\max}) > B_C(\infty) = 0$ it follows from Eq. (11) that

345 $$B_C > I_{r,0}^{-1}(\beta_{\max}) - 1 = \frac{\hat{I}_{\text{mono}}}{\hat{I}_{\text{bist}}(\beta_{\max})} - 1, \tag{12}$$

i.e. the enhancement B_C is at least as large as the relative difference between the monostatic and the bistatic backscatter, $\hat{I}_{\text{mono}}$ and $\hat{I}_{\text{bist}}$, at the largest available bistatic angle $\beta_{\max}$.

To fit the model, we used winter data from the accumulation area (Sect. 2.2.1). From these, we removed 14 acquisitions for which TanDEM-X instead of TerraSAR-X acted as transmitter, resulting in slightly different antenna pattern that could not be
350 compensated through the calibration, especially in the HH polarization. To determine the optimal value of the parameter pair (Λ_T, Λ_A), and the 95% confidence intervals, we used the TRF method (Sect. 2.3.1), and set the starting parameter of (Λ_T, Λ_A) to $(2\,\text{m}, 20\,\text{m})$. However, a sampling of the $\text{RMSE}[\hat{I}_{\text{r},0}(\beta) - I_{\text{r},0}(\beta)]$ in the parameter space of Λ_T, Λ_A around the optimal value revealed that the global minimum is weakly constrained, and solutions across a large span of values of Λ_A provide an acceptably low RMSE value. Thus, to explore multiple parameter pair values, we sampled a range of values of Λ_A, and used a
355 downhill simplex method implemented in the `amoeba` IDL function (Nelder and Mead, 1965) to determine the corresponding Λ_T.

3 Results

3.1 Ground-based observations - KAPRI

Figure 7 shows the observed intensity ratio $\hat{I}_{\text{r},\infty}(\beta)$ defined by Eq. (10) for the HH and VV polarizations, and the least-squares
360 best fit of the model defined by Eqs. (6), (8), and (9).

For the summer dataset, the large confidence interval and flat profile of the curve indicate the lack of presence of backscatter enhancement, while for the winter dataset a clear intensity peak is detected, with a HWHM of approx. $0.25°$ and amplitude of approx. 0.5 ($1.8\,\text{dB}$), corresponding to $\Lambda_T \approx 0.4 \pm 0.1\,\text{m}$ for the HH and VV polarization. The derived absorption lengths Λ_A are much longer than the scattering lengths with $\Lambda_A \approx 11 \pm 7\,\text{m}$ for the HH polarization and $\Lambda_A \approx 19 \pm 12\,\text{m}$ for the VV
365 polarization.

Figure 8 shows the RMSE of the model fit for the VV polarization dataset, dependent on values of the fit parameters Λ_T, Λ_A. A clear global minimum can be found in the 2-dimensional parameter space at the best-fit parameter values mentioned above, with RMSE of approximately 0.11. Residuals of the model fits for selected values of parameters Λ_T, Λ_A are shown in supplementary Fig. S1.

370 ### 3.2 Satellite observations - TanDEM-X

3.2.1 Jungfrau-Aletsch region

The large number and coverage of the TanDEM-X scenes allows an analysis of the dependency of $\hat{I}_{\text{r},0}$ on β for different land cover types. In Fig. 9, where the color of data points refers to I_{mono} (Fig. 10) to distinguish between dry and wet snow, only $\hat{I}_{\text{r},0}$ in the accumulation area $> 3500\,\text{m}$ (a, b) shows a significant dependence on β: the ratio $\hat{I}_{\text{r},0}(\beta)$ forms a clear peak that shows
375 some rounding between $\beta = 0$ and $0.05°$, characteristic of weak absorption. For both polarizations, VV and HH, and only for dry snow conditions, at the largest available bistatic angles $\beta_{\max} = 0.2°$ the bistatic backscatter intensity $\hat{I}_{\text{bist}}$ is reduced by
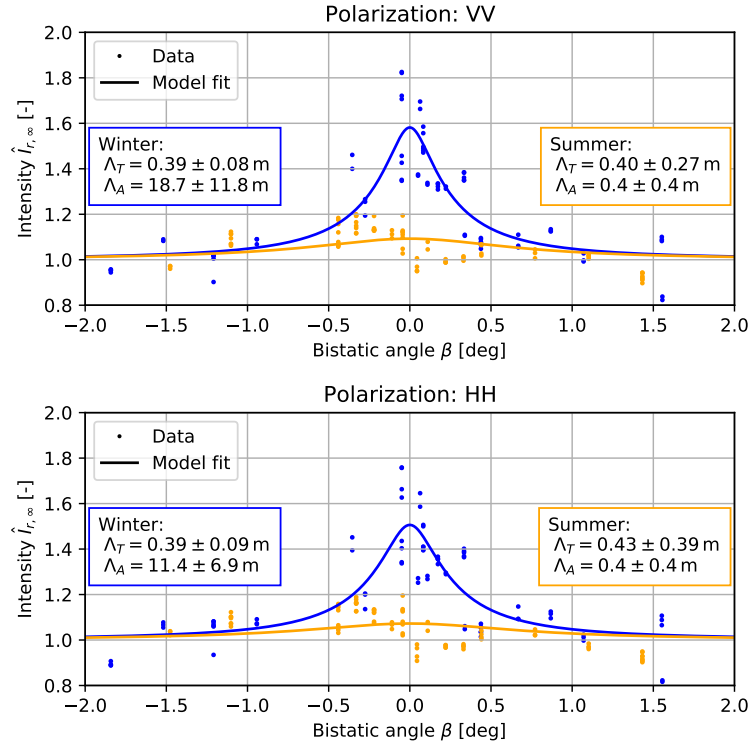
Figure 7. Intensity ratio $\hat{I}_{r,\infty}(\beta)$ observed during the ground-based experiment (KAPRI), showing backscatter enhancement in the winter dataset (blue). The observed intensities $\hat{I}(\beta)$ were averaged over the whole region of interest, for both the VV and the HH polarization. The blue and orange lines describe the least-squares fit model defined by eqs. (6), (8), and (9) for winter and summer respectively. The colored box for each dataset shows the best-fit value, and the 95% confidence interval for the model parameters Λ_T, Λ_A describing the scattering and absorption mean free paths.

approximately 20% compared to $\hat{I}_{\text{mono}}$. For wet snow no reduction of $\hat{I}_{r,0}$ is observed at β_{max}. In contrast, neither the ablation area of Great Aletsch Glacier, Fig. 9(c), nor areas covered by conifer forest, Fig. 9(d), show any significant dependence of $\hat{I}_{r,0}$ on β.

380   To investigate the spatial distribution of areas that show enhanced backscattering, Fig. 11 shows imagery of the monostatic-to-bistatic backscatter ratio $\hat{I}_{r,0}^{-1}$ together with the radar brightness I_{mono} for a series of three acquisitions with $\beta = \beta_{\text{max}}$ at the onset of snow melt in April/May 2015: On 24 April (Fig. 11a, d), backscatter enhancement is visible for a considerable amount of the area, corresponding to glaciers at high altitude ($> 3000\,\text{m}$). On 05 May (Fig. 11b, e), the backscatter enhancement is limited to high altitudes, because snow melt is occurring up to an altitude of ˜3300 m. On 07 June (Fig. 11c, f), snow melt

385   reaches the peaks of the highest mountains (4274 m) and no enhanced backscattering is detectable at any place.

To estimate the scattering and absorption parameters Λ_T and Λ_A, as well as the peak width and the backscatter enhancement, we fitted the model, Eq. (11), to the dry firn data of the accumulation area, constrained to winter acquisitions (the selection is
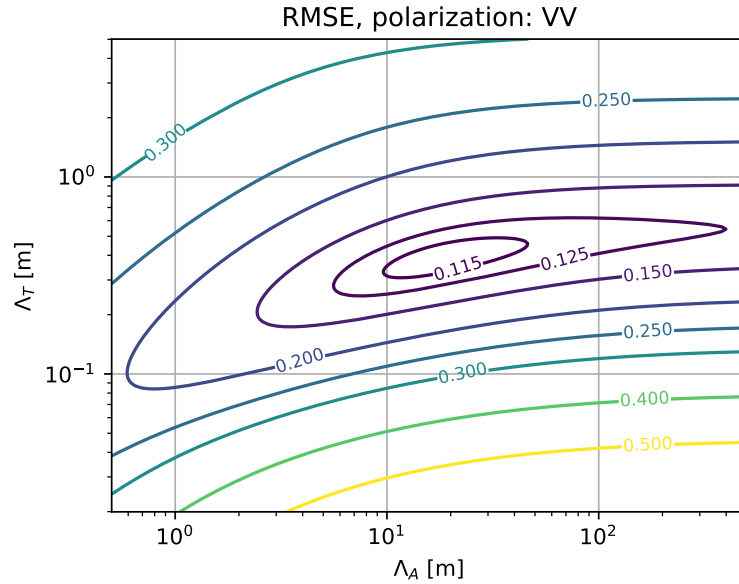
Figure 8. Contour plot of root mean square error (RMSE) between measured and modeled winter data in Ku-band (Fig. 7) for different parameter pairs Λ_A, Λ_T. The plot indicates a clear global minimum because the CBOE peak height, and hence Λ_A, can be well estimated due to the availability of ground-based KAPRI measurements at large bistatic angles $\beta > 1°$.

specified in Sect. 2.3.2 and indicated by gray shading in Fig. 10a). Figure 12(a, b) shows the selected dataset at two different scales of β. The solution with the minimal RMSE value is indicated by the black dashed line. This solution corresponds to $\Lambda_T = 2.16 \pm 0.36\,\mathrm{m}$ and $\Lambda_A = 21.77 \pm 2.72\,\mathrm{m}$ (95% confidence interval, VV polarization), an enhancement of $B_C = 35\%$ (+1.3 dB), and a HWHM of the peak of $0.12°$. For the HH polarization (not shown) we obtained $\Lambda_T = 1.62 \pm 0.35\,\mathrm{m}$ and $\Lambda_A = 25.88 \pm 5.27\,\mathrm{m}$, corresponding to $B_C = 41\%$ (+1.5 dB), and a HWHM of $0.14°$.

Figure 12(a) also illustrates that the available data, sampled with a limited range of bistatic angles, allows multiple model solutions with similar RMSE values (colored lines). The solutions are parametrized by different pairs of scattering and absorption mean free paths Λ_T, Λ_A and were determined by finding Λ_T for a fixed Λ_A. Table 1 summarizes these parameter pairs and lists for each solution the modeled peak characteristics and the RMSE with respect to the measured data.

Figure 12(b) illustrates how the different model solutions asymptotically reach the incoherent background $I_{r,0}(\beta \to \infty)$ at large bistatic angles. The sampling of larger bistatic angles would reveal whether significantly lower values of $I_{r,0}(\beta)$ than observed exist, and would, therefore, allow for a better constraint of the model parameters.

A contour map of the RMSE between the measured and the modeled values (VV) is shown in Figure 13. While the shallow global minimum (RMSE = 0.0106) is located at the optimal solution $\Lambda_T = 2.12\,\mathrm{m}, \Lambda_A = 21.8\,\mathrm{m}$, multiple other solutions exist, that show only slightly higher RMSE values between 0.011 and 0.015 (see also Table 1). This set of possible parameter
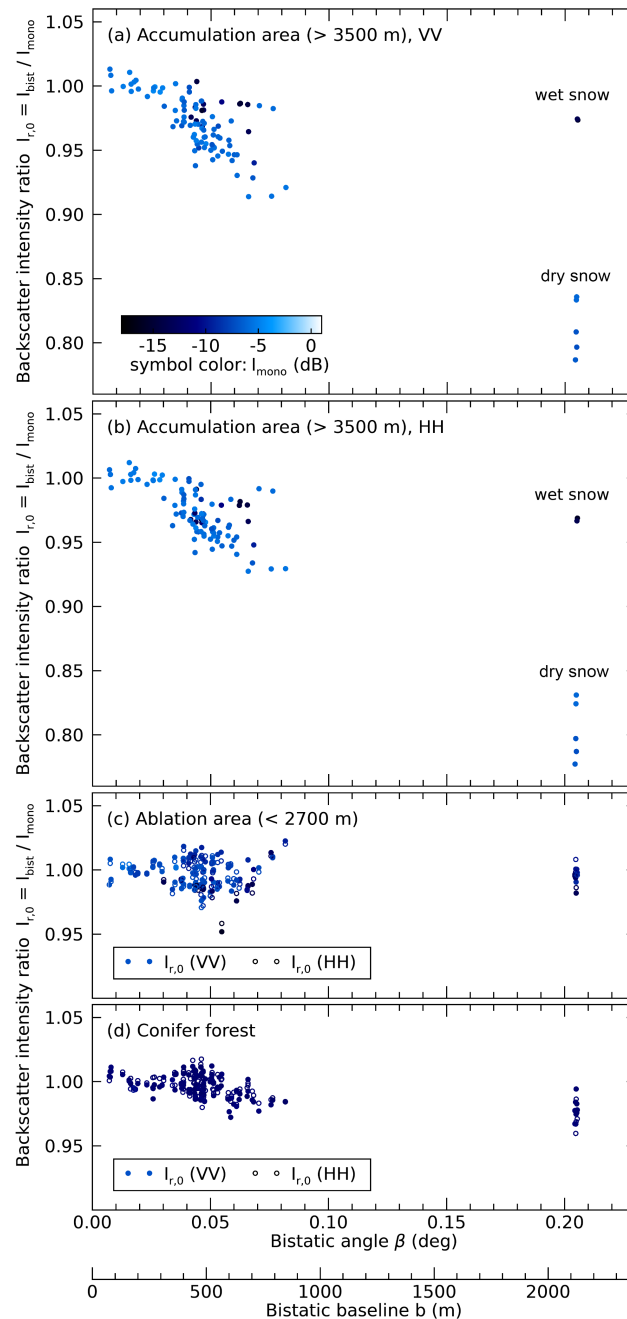
Figure 9. (a,b) The intensity ratio $\hat{I}_{r,0}$ observed by the satellite TanDEM-X in the accumulation area. Backscatter enhancement is indicated by the significant dependence of $\hat{I}_{r,0}$ on the bistatic angle β for dry-snow observations in both polarizations (VV, HH). The symbol color indicates the monostatically measured radar brightness I_{mono} and helps to differentiate between wet snow (dark blue) and dry snow (light blue), see Fig. 10(a). (c): The ablation area of Great Aletsch Glacier, located below 2700 m, is covered by $0 - 3\,\mathrm{m}$ of snow in winter but does not show any dependence of $\hat{I}_{r,0}$ on β. (d) areas covered by conifer forest show no significant dependence on β.
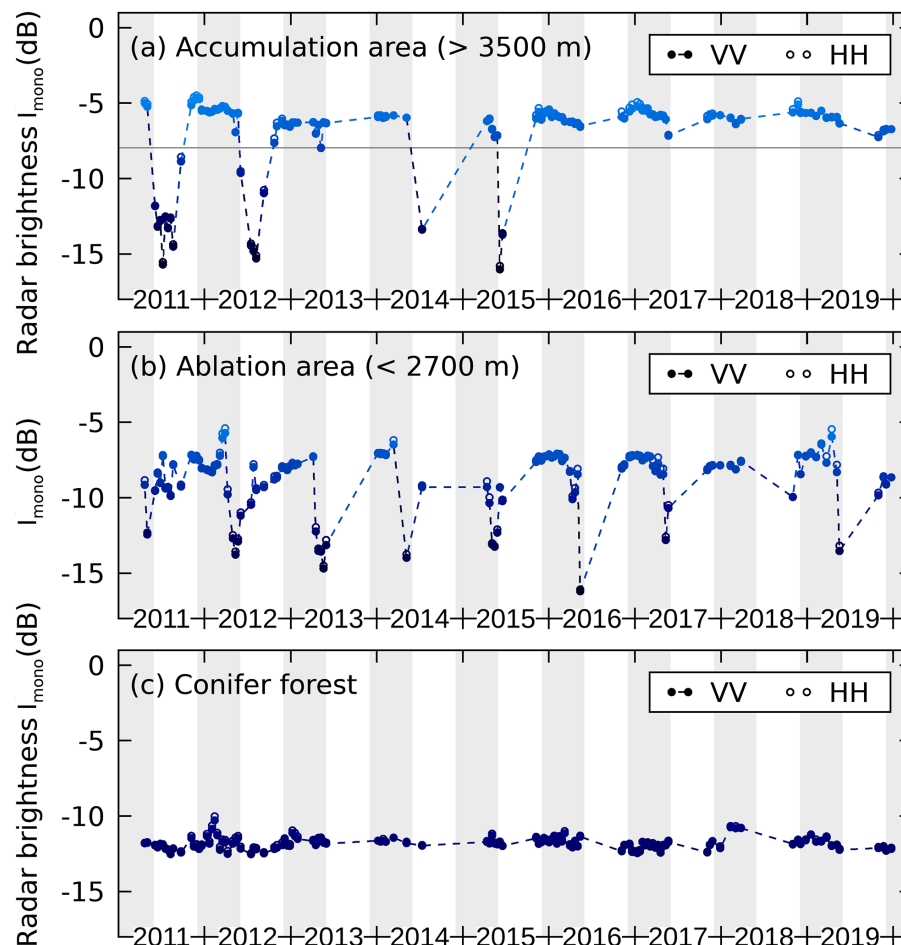
Figure 10. Time series of the monostatically measured radar brightness $\hat{I}_{\mathrm{mono}}$ observed by the satellite TanDEM-X for three different land cover types: (a) deep firn in accumulation area above 3500 m, (b) the tongue of Great Aletsch Glacier which is covered by 0-3 m of snow in winter. In (a) and (b) seasonal variations of I_{mono} provide a good indicator to distinguish between dry and wet snow. Gray shading indicates the period 01 December–31 May when dry firn is most likely present in the accumulation zone (supported by the horizontal gray line). This period was selected for estimation of the absorption and scattering lengths Λ_A and Λ_T. A backscatter difference between the VV and HH polarization is hardly visible. (c) Compared to snow, forest (mainly conifer forest) shows only small variations of the radar brightness when summer and winter acquisitions are available (2011–2013).
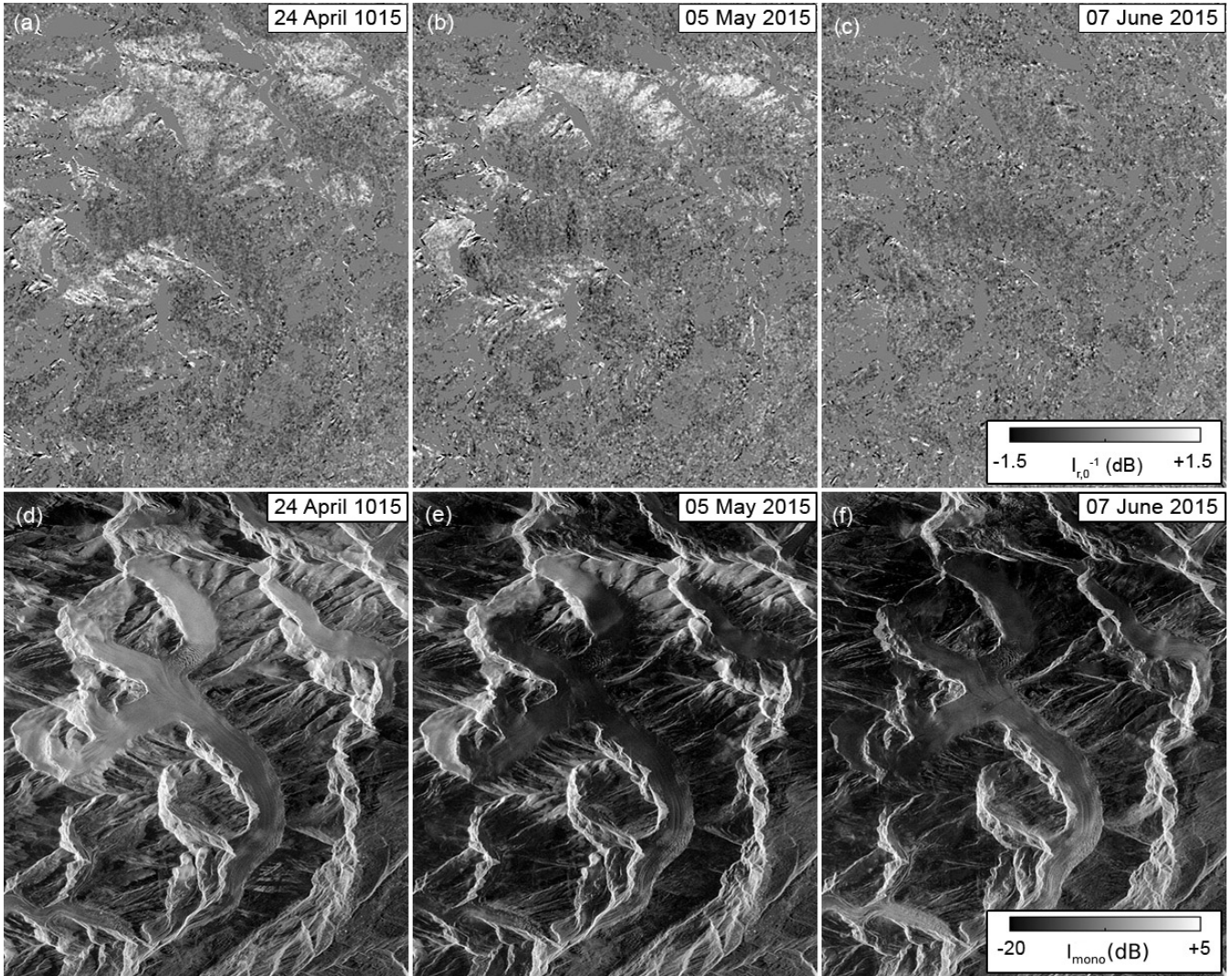
Figure 11. (a-c): monostatic-to-bistatic backscatter ratio $\hat{I}_{r,0}^{-1}$, observed by TanDEM-X at the largest available bistatic angles $\beta_{\max} = 0.2°$ before and during snow melt. (d-f): radar brightness for the same dates. Areas covered by wet snow appear dark. Great Aletsch Glacier is flowing clockwise from top to bottom. In (a, b), high altitude areas (above 3000 m and above 3400 m) show backscatter enhancement. In (c) wet snow is present in the entire scene and absorption prevents the CBOE. In (f) an increase of the backscatter intensity becomes visible on the tongue of Great Aletsch Glacier and on nearby vegetation covered slopes, indicating that in these areas all snow has melted. Images are shown in slant range/azimuth coordinates.

pairs (Λ_A, Λ_T) forms a non-linear curve (1-dimensional manifold) in the 2-dimensional parameter space (red "+"-symbols in Figure 13).
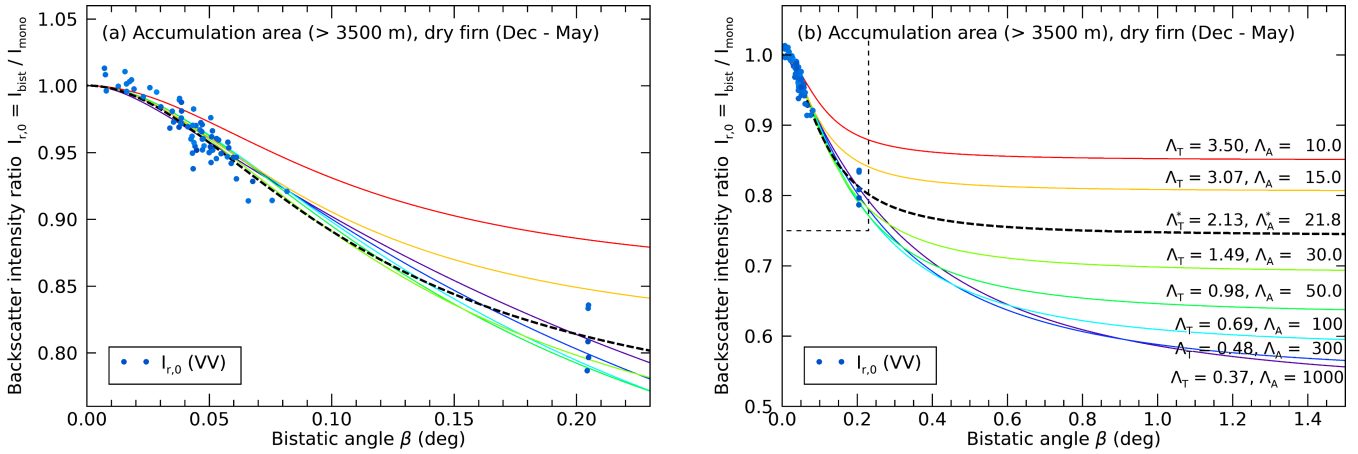
Figure 12. (a): Backscatter ratios $\hat{I}_{r,0}(\beta)$ (dots) restricted to dry firn observations in winter (01 December–31 May; $I_{mono} > -8\,\mathrm{dB}$) in the accumulation areas of the Jungfrau-Aletsch region from TanDEM-X in the VV polarization. Colored lines indicate different CBOE model curves, Eq. (11), parametrized by a range of scattering and absorption parameter combinations (Λ_T, Λ_A) that can describe the data to different degrees. (b): same as (a) (in dashed box) but zoomed out to visualize at which β the different model fits converge to the flat region of the intensity curve $I_{r,0}(\beta \to \infty)$ where coherent backscatter is negligible. Measurements at larger bistatic angles $\beta > 0.5°$ could substantially better constrain the total peak height (and thereby Λ_A) but such large angles are currently not available.

Λ_A (m)	Λ_T (m)	$B_C(0)$	HWHM (deg)	RMSE
1000	0.37	0.92	0.28	0.0111
300	0.48	0.85	0.25	0.0117
100	0.69	0.72	0.21	0.0129
50	0.98	0.59	0.17	0.0129
30	1.49	0.45	0.14	0.0116
25.9	**1.63**	**0.41**	**0.14**	**0.0103** (HH)
21.8	**2.13**	**0.35**	**0.12**	**0.0106** (VV)
15	3.08	0.24	0.10	0.0145
10	3.50	0.18	0.11	0.0257

Table 1. Scattering length Λ_T, peak height $B_C(0)$, and peak width (HWHM) for a set of chosen absorption lengths Λ_A determined from the TanDEM-X dataset (VV) of dry firn in the high altitude accumulation area. The bold lines indicate the optimal parameter pair for the VV and HH polarization. RMSE is the root mean square error between the measured and the modeled value of $I_{r,0}$.

405 3.2.2 Teram-Shehr/Rimo Glacier

Due to the limited amount of acquisitions of the Teram-Shehr and Rimo glacier we only briefly summarize here some observations and refer to the supplementary figures S9–S11 for details. In the accumulation area $> 6100\,\mathrm{m}$, we observed backscatter ratios $\hat{I}_{r,0}(\beta)$ between 0.72 and 0.77 in five large-baseline acquisitions with $\beta = 0.193°$ from orbit 75 between 11 May and
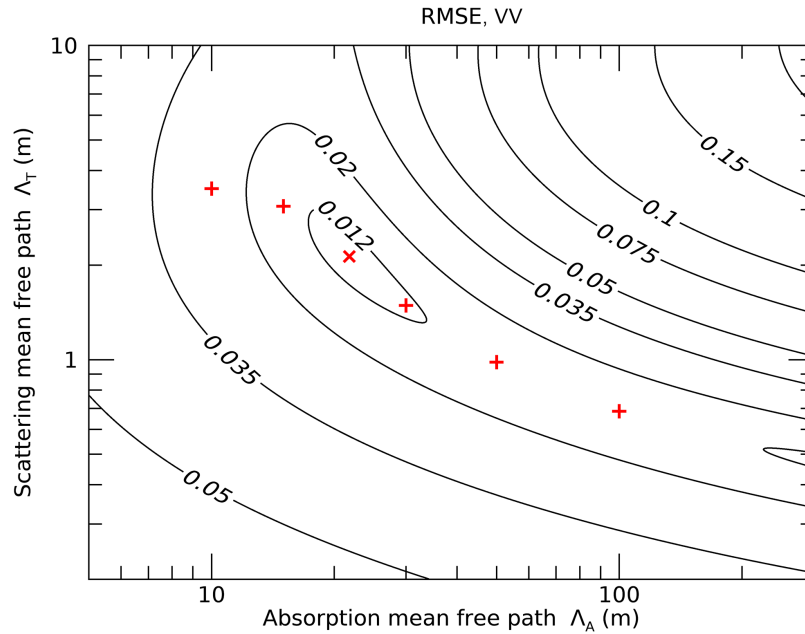
Figure 13. Contour map of root mean square error (RMSE) between measured and modeled data for TanDEM-X (Fig. 12) for different pairs of Λ_A, Λ_T. The plot shows a weak global minimum because acquisitions at sufficiently large β, that could better constrain Λ_A, were not currently available. The model parameters and RMSE values for the red "+" symbols are given in Table 1. For these points, the parameter value of Λ_T was estimated by nonlinear least squares minimization for different choices of Λ_A.

24 June 2015. For orbit 98 with $\beta = 0.231°$, we observed ratios $\hat{I}_{r,0}(\beta)$ between 0.74 and 0.81 between 01 May and 03 June 2015. With Eq. (12) these values allow estimating an lower limit for the backscatter enhancement B_C and correspond to an enhancement of at least 23–39% (+0.9 to +1.4 dB). In comparison, for the Jungfrau-Aletsch region, we obtain a lower limit of 19–27% (+0.8 to +1.0 dB). Due to weak model constraints in the Teram-Shehr dataset, we do not provide parameters estimated by model fits.

4 Discussion

4.1 Cause of enhancement: CBOE vs. SHOE

In both Ku-band and X-band observations of terrestrial snow, we observed narrow intensity peaks with an angular width of a fraction of 1°. These peaks are clearly attributable to the CBOE as opposed to the SHOE, which follows from a comparison of the effects' properties as described by Hapke (2012, Chapter 9):

Firstly, the SHOE requires that the scatterers are much larger than the wavelength of the incident radiation so that they can cast sharp shadows. This requirement can hardly be fulfilled at radar wavelengths of several centimeters, since ice particles in snow have average diameters on the order of millimeters (Kuga et al., 1991). A grain size of $0.3 - 1.5\,\mathrm{mm}$ was observed

in the seasonal snowpack studied by the KAPRI experiment (Fig. 2). The snowpack did not show any cm-sized ice structures
that could have been caused by strong melt-events. Furthermore, the narrow peak width is in agreement with characteristics
of the CBOE, while a SHOE peak usually has a width of several degrees or tens of degrees, depending on particle size
425   distribution. Finally, SHOE is only present in media where single scattering is dominant. Multiple scattering processes decrease
the amplitude of the SHOE and increase amplitude of the CBOE. Since dry snow is a weakly absorbing medium for microwaves
where multiple (i.e. volume) scattering is considerable (Kuga et al., 1991), the CBOE is expected to be the dominant effect.

4.2 Observations of CBOE

4.2.1 Ground-based observations - KAPRI

430   Figure 7 shows a statistically significant enhancement peak for the winter acquisition, and a lack of such a peak for the
summer dataset, which was acquired using an identical target region of interest, identical acquisition procedure (except platform
substitution to allow movement on snow/road), and identical processing pipeline. The summer dataset thus serves as a useful
control which ensures that the detected enhancement peak is not an erroneous artifact of the bistatic data processing pipeline,
and it also indicates that the enhancement peak is indeed caused by the snow layer present on the hillside. The absence of an
435   enhancement peak in summer leads (in accordance with the red line in Fig. 6) to estimates of comparable values $\Lambda_T \approx \Lambda_A$. In
the context of the model, an absorption length as short as the scattering length suppresses higher-order scattering paths, and
thus is equivalent to a dominant single-scattering process.

   The best-fit values of model parameters in Fig. 7 indicate a scattering mean free path value Λ_T between 30 and 50 cm, and
an absorption length Λ_A between 6 and 24 m for both polarizations. No statistically significant difference of the parameter
440   estimates is observed between the HH and VV polarizations. This is well-aligned with the theoretical model of Mishchenko
(1992), in which there is only a very small difference between the co-polarized backscatter enhancement factors for these two
polarizations. The HWHM of the angular peak of $\approx 0.25°$ is sufficiently wide so that KAPRI's transmit antennas' non-zero
size, which limits the angular resolution to $0.05°$ (Sect. 2.1.2), has only a very limited effect on the precision with which the
width and height of the peak can be determined.

445   The thickness of the snow layer during the winter acquisitions was measured on-site as approximately 1.5 m (Fig. 2), and
thus the estimate of Λ_A is several times higher than the snow layer thickness. The extremely shallow local incidence angle
(above $70°$ for the vast majority of the ROI area) and short transport mean free path Λ_T would likely lead to longer trajectories
of the radiation through the snow medium before reaching the ground layer. Nevertheless, the snowpack's thickness of only
3–4 scattering mean free paths could result in higher order scattering being limited by the snow depth. Missing higher order
450   scattering, in turn, is an explanation for a rounding of the peak shape (Akkermans et al., 1988, Fig. 7). During the field
experiment, a corner reflector at the bottom of a 1.55 m deep snow pit was still visible, indicating that at least a fraction of
microwaves reached the ground, thereby limiting higher order scattering.

4.2.2 Satellite observations - TanDEM-X

A significant dependence of the backscatter intensity on the bistatic angle, $\hat{I}_{r,0}(\beta)$, is only visible in the accumulation zones of

455   the Jungfrau-Aletsch region with altitude $H > 3500\,\mathrm{m}$ (Fig. 9a, b). Above this altitude, a firn layer with below freezing snow temperatures is present to a depth of several tens of meters (Haeberli and Alean, 1985; Suter et al., 2001). This thick and cold firn layer represents a disordered medium where multiple scattering is possible and at the same time microwave absorption is weak, because liquid water is absent. The existence of the CBOE in dry firn is further supported by the spatial and temporal distribution of an enhanced brightness ratio $\hat{I}_{r,0}$. Spatially, the enhancement matches to the accumulation area of high altitude

460   glaciers – in the Jungfrau-Aletsch region (Fig. 11) as well as for Teram-Shehr/Rimo glacier the Karakorum (Figs. S10 and S11). Temporally, the backscatter enhancement vanishes in these areas when snow melt sets in and thus the scattering predominantly takes place at the snow surface.

The rounding of the peak shape in Fig. 12(a) indicates that either weak absorption or a limited thickness of firn is present in the accumulation area. Field measurements indicate cold firn in at least the upper $8\,\mathrm{m}$ (Bannwart, 2021) and literature data

465   indicate that temperate firn might be present at around $15\,\mathrm{m}$ below the surface (Suter et al., 2001). The global minimum at $\Lambda_A = 21.8\,\mathrm{m}$ in Fig. 13 might therefore provide a realistic estimate for Λ_A as larger absorption lengths are difficult to conform to field measurements.

On the tongue of Great Aletsch Glacier, where a seasonal snowpack is present during winter, no backscatter enhancement was observed in X-band (Fig. 9c). As seasonal snow is younger than multi-year firn, smaller snow grain sizes are expected,

470   resulting in longer scattering lengths compared to the accumulation area where we observed $\Lambda_T = 2.1\,\mathrm{m}$. Considering the thickness of the seasonal snowpack of 0–3 m, these longer scattering lengths would correspond to on average less than 2–3 scattering events for the two-way travel through the snowpack. In consequence, the single scattering at the snow-ice interface at the bottom of the snowpack can remain the dominant scattering process. The low average number of scattering events in the seasonal snow volume is, therefore, not sufficient for the CBOE to occur on the ablation area of Great Aletsch Glacier.

475   In forest covered areas, no significant dependency of $\hat{I}_{r,0}$ on β is visible. We think the reason is that, compared to dry snow, multiple scattering at X-band is reduced in forest due to absorption of microwaves, hence the CBOE is prevented.

4.2.3 Comparison of bistatic measurement geometries

The KAPRI experiment sampled a larger range of bistatic angles (up to $1.92°$) so that the flat incoherent intensity background I_0 could be sampled. Therefore, both the width and the height of the enhancement peak in winter can be constrained much better

480   than with the TanDEM-X observations where $\beta_{max} \approx 0.2°$. This, in turn, translates to better constrained estimates of parameters Λ_T and Λ_A as illustrated by the clearly visible global minimum in the plot of the RMSE value in Fig. 8 as compared to Fig. 13.

Compared to the KAPRI experiment, the bistatic angles sampled by TanDEM-X are relatively small, making it possible that not the entire peak of the CBOE has been sampled. In consequence, the bistatic data at $\beta_{max} = 0.2°$ might still be affected by the CBOE. Missing measurements at larger bistatic angles result in a weak constraint of the parameter pair (Λ_T, Λ_A), permitting a

485   range of value pairs that each can fit the data (Table 1 and Figs. 12 and 13). To better constrain the observed values of Λ_T, Λ_A,

bistatic angles of at least $\beta = 0.5°$ would need to be sampled by TanDEM-X. However, such larger angles are currently not available.

4.3   Impact of the CBOE on backscatter observations

Generally, the existence of a narrow backscatter enhancement peak around the monostatic direction needs to be kept in mind by
490   all researchers performing backscatter measurements of snow, regardless of whether the used sensors are considered monostatic or bistatic. On one hand, for truly monostatic sensors the CBOE is strongest. On the other hand, some radar sensors are considered as monostatic even though they have a small but non-zero spatial separation between the transmitting and receiving antennas. Due to this bistatic baseline, the detected backscatter intensity value could be significantly reduced compared to the value that would have been detected by a truly monostatic sensor. When prior estimates of Λ_T and Λ_A over a particular medium
495   are available, Eq. (6) could be used to estimate the width and height of the peak, which can subsequently be used to estimate bistatic angle values where the CBOE affects the measurements.

As an example of the necessity to precisely align the measurement geometry to the expected width of the peak, Tan et al. (2015) compared modeled results to active and passive microwave measurements at X- to Ka-band performed in Finland, Sodankylae as part of the NoSREx field experiment (Lemmetyinen et al., 2016). The active measurements were performed
500   with the SnowScat instrument (Wiesmann et al., 2010). The model, which includes backscatter enhancement into the DMRT theory, might provide a significant step forward for modeling of the radar backscatter signal from snow. However, if the peak width of the CBOE in the NoSREx experiment is comparable to the narrow observed peak widths in our study, the bistatic angles of the SnowScat measurements would actually be one order of magnitude too large to observe the CBOE. This follows from the instrument height of 9.6 m, the incidence angle range of 30–60° (Lemmetyinen et al., 2016), and the antenna separation
505   of 72 cm (Wiesmann et al., 2010; Wiesmann and Werner, 2010), resulting in bistatic angle values $\beta = 1.8 - 3.7°$.

Except for possible extreme cases of a medium causing an extremely narrow enhancement peak (with width on the order of thousandths of a degree), the velocity-induced bistatic angle β_v of moving radar platforms is negligible in the context of the CBOE. For the side-looking geometry, the bistatic angle β_v caused by platform motion with velocity v can be calculated as $\beta_v = 2v/c$, where c is the speed of light. Thus, for all conventional sensors – even for satellite platforms in low Earth orbit
510   moving at speeds of $6-8 \, \mathrm{km \, s^{-1}}$ – the resulting value of β_v is on the order of thousandths of a degree or less.

4.4   Applications based on the CBOE

In TanDEM-X data we have observed a backscatter enhancement of at least 1.3 dB for firn covered areas of the European Alps and in the Karakorum, while for firn free areas no backscatter enhancement could be observed. This suggests that detection of deep firn with X-band is possible when large enough bistatic angles $\beta > 0.2°$ are available.
515   For seasonal snow, we observed a clear CBOE peak ($\sim 1.8 \, \mathrm{dB}$ of backscatter enhancement) at Ku-band using KAPRI whereas in X-band we were not able to observe an enhancement. The higher sensitivity of high-frequency systems (Ku- or possibly Ka-band) to detect the CBOE in seasonal snow results from the shorter scattering length, since sufficiently high-order scattering events can occur within the snow layer of limited thickness. Furthermore, the difference between KAPRI

observations in summer (no CBOE from vegetation) and winter (snow-induced CBOE) demonstrates how Ku-band bistatic

520 observations could potentially provide a mean to discriminate dry snow from vegetation and therefore provide a mean to map snow cover extent. Beyond that, the frequency dependency of the scattering lengths makes a characterization of the intensity of the CBOE at multiple frequencies possible which, in turn, could allow for a quantitative characterization of the height or water equivalent of seasonal snow. Area covered by snow, snow depth, and snow-water equivalent are considered key data products for the snow Essential Climate Variable (Belward, 2016). Bistatic missions characterizing the CBOE occurring in snow can

525 thus be an asset in mapping these data products.

In terms of polarimetric measurements, the results of this study, as well as theoretical models (Mishchenko, 1992), indicate that the effect is present predominantly in co-polarized channels, and the effect is equally strong in both horizontal and vertical polarizations. Nevertheless, in further studies the use of full-polarimetric radar systems can still be advantageous, e.g. to decisively differentiate the CBOE and the SHOE based on their different impact on linear and circular polarization ratios

530 (Rignot, 1995; Hapke, 2012, Sect. 9.4).

Existing bistatic ground-based SAR sensors (Pieraccini and Miccinesi, 2017; Wang et al., 2019), and to a certain extent also airborne bistatic SAR sensors (Dubois-Fernandez et al., 2006; Meta et al., 2018) could be employed to study the effect locally with a high temporal resolution and to observe temporal variations of the effect. Space-borne platforms, while limited by orbital mechanics and repeat-intervals, can provide a means to sample and to characterize the CBOE on the global scale.

535 Finally, our characterization of the CBOE at X- and Ku-band in terrestrial snow could inspire future inter-planetary missions, aiming to search for water ice and possibly other types of snow, to employ bistatic radar measurements.

5   Conclusions

In this paper we presented the first observations of the coherent backscatter opposition effect (CBOE) and the sampling of its angular peak shape at radio wavelengths within the Earth's cryosphere. The existence of the peak was confirmed in seasonal

540 snow cover at Ku-band wavelengths by the ground-based bistatic radar system KAPRI. With the bistatic satellite formation TanDEM-X, the effect was also confirmed at X-band within the accumulation zone of high glaciers in the European Alps and the Karakorum.

The observability of the CBOE in bistatic radar measurements of snow presents an opportunity for future satellite missions aiming to derive snow properties from synthetic aperture radar data on the global scale. The radiometric precision requirement

545 for such a spaceborne radar system is demanding, since the theoretical maximal amplitude of the effect is 3 dB – in this study, we were able to characterize the peak using TanDEM-X and data-driven radiometric calibration. Deployment of such bistatic systems – at bistatic angles up to one or two degrees, and covering the entire CBOE peak including the incoherent background – would open up a new pathway to characterize snow through microwave scattering.

The Ku-band observations presented in this paper suggest that the CBOE can be used as an indicator for presence of seasonal

550 snow cover. At X-band, the CBOE could be applied to detect dry snow thicker than several meters, e.g. multi-year firn in accumulation areas of glaciers. Furthermore, through analysis of the angular width and height of the enhancement peak,

scattering and absorption mean free paths within the snowpack can be estimated. Knowledge of the scattering mean free path and the discrimination between single (surface) and higher order (volume) scattering in areas where the CBOE is present could help to better constrain the radar penetration depth which, in turn, is crucial for precise surface height estimation by means of
555 radar altimetry and interferometry.

The CBOE thus provides a pathway towards better characterization of area covered by snow, possibly also snow depth, and snow-water equivalent, which are the three key data products for snow as an Essential Climate Variable. Furthermore, the detection and characterization of the CBOE in terrestrial snow is also an encouraging sign for applying this measurement concept in space missions which aim to confirm the presence of water ice on surfaces of other solar system bodies.

560 *Data availability.* TanDEM-X data is available from DLR at https://tandemx-science.dlr.de/ and was provided by the proposal leinss_ XTI_ GLAC6870. KAPRI SLC data, as well as data values for plots, will be published in the ETH Research Collection with the DOI 10.3929/ethz-b-000516171 while the paper is under review.

Author contributions. SL conceptualized the study of coherent backscatter enhancement in snow with bistatic radar. MS and SL designed the Davos field experiment and wrote the manuscript together. MS processed and analyzed the ground based data, SL the space borne data.
565 IH suggested exploration of bistatic radar signals with KAPRI. All authors reviewed, edited, and approved the submitted version of the manuscript.

Competing interests. The authors declare that they have no conflict of interest.

Acknowledgements. The authors would like to thank Tingting Li, Yuta Izumi, Simone Jola, and Michael Arnold for their support during field work in Davos, Emmanuel Trouvé for proofreading the manuscript, Laurane Charrier for valuable input for applications of the CBOE,
570 and Thomas Busche for support with the TanDEM-X acquisitions. The authors would also like to thank Mr. Reto Müller for access to his property during acquisitions and the staff of Bergbahnen Rinerhorn AG for assistance with equipment transportation. The TanDEM-X data was provided by the German Aerospace Center (DLR) via proposal XTI_GLAC6780. SL was supported by the French ministry of Europe and foreign affairs, within the framework of the 'Make Our Planet Great Again' program for postdoctoral researchers.

References

575 Aegerter, C. M. and Maret, G.: Coherent Backscattering and Anderson Localization of Light, in: Progress in Optics, vol. 52, pp. 1–62, Elsevier, https://doi.org/https://doi.org/10.1016/S0079-6638(08)00003-6, 2009.

Agarwal, V., Bolch, T., Syes, T. H., Pieczonka, T., Strozzi, T., and Nagaich, R.: Area and mass changes of Siachen Glacier (East Karakoram), Journal of Glaciology, 63, 148–163, https://doi.org/10.1017/jog.2016.127, 2017.

Akkermans, E., Wolf, P. E., and Maynard, R.: Coherent backscattering of light by disordered media: Analysis of the peak line shape, Physical
580 review letters, 56, 1471, 1986.

Akkermans, E., Wolf, P., Maynard, R., and Maret, G.: Theoretical study of the coherent backscattering of light by disordered media, Journal de Physique, 49, 77–98, https://doi.org/10.1051/jphys:0198800490107700, 1988.

Baffelli, S., Frey, O., Werner, C., and Hajnsek, I.: Polarimetric Calibration of the Ku-Band Advanced Polarimetric Radar Interferometer, IEEE Transactions on Geoscience and Remote Sensing, 56, 2295–2311, 2017.

585 Bannwart, J.: Personal communication, 2021.

Belward, A. e. a.: The global observing system for climate: implementation needs, Tech. Rep. GCOS-200, World Meteorological Organization, 2016.

Black, G. J., Campbell, D. B., and Nicholson, P. D.: Icy Galilean Satellites: Modeling Radar Reflectivities as a Coherent Backscatter Effect, Icarus, 151, 167–180, https://doi.org/10.1006/icar.2001.6616, 2001.

590 Dubois-Fernandez, P., Cantalloube, H., Vaizan, B., Krieger, G., Horn, R., Wendler, M., and Giroux, V.: ONERA-DLR bistatic SAR campaign: Planning, data acquisition, and first analysis of bistatic scattering behavior of natural and urban targets, Radar, Sonar and Navigation, IEE Proceedings -, 153, 214– 223, https://doi.org/10.1049/ip-rsn:20045117, 2006.

Duque, S., Balss, U., Rossi, S., Fritz, T., and Balzer, W.: TanDEM-X Payload Ground Segment CoSSC Generation and Interferometric Considerations, TD-PGS-TN-3129, issue 1.0, Remote Sensing Technology Institute, DLR, 2012.

595 Fierz, C., Armstrong, R., Durand, Y., Etchevers, P., Greene, E., McClung, D., Nishimura, K., Satyawali, P., and Sokratov, S.: The International Classification for Seasonal Snow on the Ground, 2009.

Fritz, T., Brautigam, B., Krieger, G., and Zink, M.: TanDEM-X Ground Segment - TanDEM-X Experimental Product Description, TD-GS-PS-3028, issue 1.2, DLR, 1.2 edn., 2012.

Haeberli, W. and Alean, J.: Temperature and Accumulation of High Altitude Firn in the Alps, Annals of Glaciology, 6, 161–163,
600 https://doi.org/10.3189/1985AoG6-1-161-163, 1985.

Hajnsek, I., Busche, T., Krieger, G., Zink, M., Schulze, D., and Moreira, A.: Announcement of opportunity: TanDEM-X science phase, Tech. Rep. TD-PD-PL-0032, Microwave and Radar Institute (DLR-HR), 2014.

Hapke, B.: Bidirectional reflectance spectroscopy: 4. The extinction coefficient and the opposition effect, Icarus, 67, 264–280, https://doi.org/https://doi.org/10.1016/0019-1035(86)90108-9, 1986.

605 Hapke, B.: Coherent backscatter and the radar characteristics of outer planet satellites, Icarus, 88, 407–417, https://doi.org/10.1016/0019-1035(90)90091-M, 1990.

Hapke, B.: Theory of Reflectance and Emittance Spectroscopy, Cambridge University Press, 2 edn., https://doi.org/10.1017/CBO9781139025683, 2012.

Hapke, B., DiMucci, D., Nelson, R., and Smythe, W.: The cause of the hot spot in vegetation canopies and soils: Shadow-hiding versus
610 coherent backscatter, Remote Sensing of Environment, 58, 63–68, https://doi.org/https://doi.org/10.1016/0034-4257(95)00257-X, 1996.

Hapke, B., Nelson, R., and Smythe, W.: The Opposition Effect of the Moon: Coherent Backscatter and Shadow Hiding, Icarus, 133, 89–97, https://doi.org/10.1006/icar.1998.5907, 1998.

Hapke, B. W., Nelson, R. M., and Smythe, W. D.: The Opposition Effect of the Moon: The Contribution of Coherent Backscatter, Science, 260, 509–511, https://doi.org/10.1126/science.260.5107.509, 1993.

615 Jun, L., Wang, W., and Zwally, H. J.: Interannual variations of shallow firn temperature at Greenland summit, Annals of Glaciology, 35, 368–370, 2002.

Kaasalainen, S., Kaasalainen, M., Mielonen, T., Suomalainen, J., Peltoniemi, J. I., and Näränen, J.: Optical properties of snow in backscatter, Journal of Glaciology, 52, 574–584, https://doi.org/10.3189/172756506781828421, 2006.

Krieger, G., Moreira, A., Fiedler, H., Hajnsek, I., Werner, M., Younis, M., and Zink, M.: TanDEM-X: A satellite formation for high-resolution
620 SAR interferometry, IEEE Transactions on Geoscience and Remote Sensing, 45, 3317–3341, 2007.

Kuga, Y. and Ishimaru, A.: Retroreflectance from a dense distribution of spherical particles, Journal of the Optical Society of America A, 1, 831, https://doi.org/10.1364/josaa.1.000831, 1984.

Kuga, Y., Ulaby, F. T., Haddock, T. F., and DeRoo, R. D.: Millimeter-wave radar scattering from snow 1. Radiative transfer model, Radio Science, 26, 329–341, https://doi.org/10.1029/90RS02560, 1991.

625 Leinss, S. and Bernhard, P.: TanDEM-X:Deriving InSAR Height Changes and Velocity Dynamics of Great Aletsch Glacier, IEEE Journal of Selected Topics in Applied Earth Observations and Remote Sensing, 14, 4798–4815, https://doi.org/10.1109/JSTARS.2021.3078084, 2021.

Lemmetyinen, J., Kontu, A., Pulliainen, J., Vehviläinen, J., Rautiainen, K., Wiesmann, A., Mätzler, C., Werner, C., Rott, H., Nagler, T., Schneebeli, M., Proksch, M., Schüttemeyer, D., Kern, M., and Davidson, M. W.: Nordic Snow Radar Experiment, Geoscientific Instru-
630 mentation, Methods and Data Systems, 5, 403–415, https://doi.org/10.5194/gi-5-403-2016, 2016.

Lucas, C., Leinss, S., Bühler, Y., Marino, A., and Hajnsek, I.: Multipath interferences in ground-based radar data: A case study, Remote Sensing, 9, 1–19, https://doi.org/10.3390/rs9121260, 2017.

Meta, A., Trampuz, C., Coccia, A., Placidi, S., Hendriks, L. I., Davidson, M., and Schuettemeyer, D.: Bistatic Airborne SAR Acquisitions at L-Band by MetaSensing: First Results, in: EUSAR 2018; 12th European Conference on Synthetic Aperture Radar, pp. 1–5, 2018.

635 Mishchenko, M. I.: Polarization characteristics of the coherent backscatter opposition effect, Earth, Moon and Planets, 58, 127–144, https://doi.org/10.1007/BF00054650, 1992.

Mishchenko, M. I., Luck, J.-M., and Nieuwenhuizen, T. M.: Full angular profile of the coherent polarization opposition effect, Journal of the Optical Society of America A, 17, 888, https://doi.org/10.1364/JOSAA.17.000888, 2000.

Montgomery, W. W. and Kohl, R. H.: Opposition-effect experimentation, Optics Letters, 5, 546, https://doi.org/10.1364/OL.5.000546, 1980.

640 Muhleman, D. O., Butler, B. J., Grossman, A. W., and Slade, M. A.: Radar images of mars, Science, 253, 1508–1513, https://doi.org/10.1126/science.253.5027.1508, 1991.

Mätzler, C. and Wegmüller, U.: Dielectric properties of freshwater ice at microwave frequencies, J. Phys. D: Appl. Phys., 20, 1623, https://doi.org/http://dx.doi.org/10.1088/0022-3727/20/12/013, 1987a.

Mätzler, C. and Wegmüller, U.: Dielectric properties of freshwater ice at microwave frequencies - Errata, J. Phys. D: Appl. Phys., 20, 1623,
645 http://stacks.iop.org/0022-3727/20/i=12/a=013, 1987b.

Nelder, J. A. and Mead, R.: A simplex method for function minimization, The computer journal, 7, 308–313, 1965.

Nozette, S., Lichtenberg, C. L., Spudis, P., Bonner, R., Ort, W., Malaret, E., Robinson, M., and Shoemaker, E. M.: The Clementine bistatic radar experiment, Science, 274, 1495–1498, https://doi.org/10.1126/science.274.5292.1495, 1996.

Oliver, C. and Quegan, S.: Understanding synthetic aperture radar images, SciTech Publishing, 2004.

650   Palmer, E. M., Heggy, E., and Kofman, W.: Orbital bistatic radar observations of asteroid Vesta by the Dawn mission, Nature Communications, 8, https://doi.org/10.1038/s41467-017-00434-6, 2017.

Patterson, G. W., Stickle, A. M., Turner, F. S., Jensen, J. R., Bussey, D. B., Spudis, P., Espiritu, R. C., Schulze, R. C., Yocky, D. A., Wahl, D. E., Zimmerman, M., Cahill, J. T., Nolan, M., Carter, L., Neish, C. D., Raney, R. K., Thomson, B. J., Kirk, R., Thompson, T. W., Tise, B. L., Erteza, I. A., and Jakowatz, C. V.: Bistatic radar observations of the Moon using Mini-RF on LRO and the Arecibo Observatory,

655   Icarus, 283, 2–19, https://doi.org/10.1016/j.icarus.2016.05.017, 2017.

Pieraccini, M. and Miccinesi, L.: Bistatic GBSAR for detecting target elevation, in: 2017 IEEE International Conference on Microwaves, Antennas, Communications and Electronic Systems (COMCAS), pp. 1–4, IEEE, 2017.

Raney, R., Freeman, T., Hawkins, R., and Bamler, R.: A plea for radar brightness, in: Proceedings of IGARSS '94 - 1994 IEEE International Geoscience and Remote Sensing Symposium, vol. 2, pp. 1090–1092 vol.2, https://doi.org/10.1109/IGARSS.1994.399352, 1994.

660   Rignot, E. J.: Backscatter model for the unusual radar properties of the Greenland ice sheet, Journal of Geophysical Research, 100, 9389–9400, https://doi.org/10.1029/95JE00485, 1995.

Rignot, E. J., Ostro, S. J., van Zyl, J. J., and Jezek, K. C.: Unusual Radar Echoes from the Greenland Ice Sheet, Science, 261, 1710–1713, https://doi.org/10.1126/science.261.5129.1710, 1993.

Simpson, R. A.: Spacecraft Studies of Planetary Surfaces Using Bistatic Radar, IEEE Transactions on Geoscience and Remote Sensing, 31,

665   465–482, https://doi.org/10.1109/36.214923, 1993.

Simpson, R. A. and Tyler, G. L.: Reanalysis of Clementine bistatic radar data from the lunar South Pole, Journal of Geophysical Research: Planets, 104, 3845–3862, https://doi.org/10.1029/1998JE900038, 1999.

Stefko, M., Frey, O., Werner, C., and Hajnsek, I.: KAPRI: A Bistatic Full-Polarimetric Interferometric Real-Aperture Radar System for Monitoring of Natural Environments, in: 2021 IEEE International Geoscience and Remote Sensing Symposium IGARSS, pp. 1950–1953,

670   https://doi.org/10.1109/IGARSS47720.2021.9553427, 2021a.

Stefko, M., Frey, O., Werner, C., and Hajnsek, I.: Calibration and Operation of a Bistatic Real-Aperture Polarimetric-Interferometric Ku-Band Radar, IEEE Transactions on Geoscience and Remote Sensing, pp. 1–1, https://doi.org/10.1109/TGRS.2021.3121466, early access, 2021b.

Suter, S. and Hoelzle, M.: Cold firn in the Mont Blanc and Monte Rosa areas, European Alps: spatial distribution and statistical models,

675   Annals of Glaciology, 35, 9–18, https://doi.org/10.3189/172756402781817059, 2002.

Suter, S., Laternser, M., Haeberli, W., Frauenfelder, R., and Hoelzle, M.: Cold firn and ice of high-altitude glaciers in the Alps: measurements and distribution modelling, Journal of Glaciology, 47, 85–96, https://doi.org/10.3189/172756501781832566, 2001.

Tan, S., Chang, W., Tsang, L., Lemmetyinen, J., and Proksch, M.: Modeling Both Active and Passive Microwave Remote Sensing of Snow Using Dense Media Radiative Transfer (DMRT) Theory with Multiple Scattering and Backscattering Enhancement, IEEE Journal of

680   Selected Topics in Applied Earth Observations and Remote Sensing, 8, 4418–4430, https://doi.org/10.1109/JSTARS.2015.2469290, 2015.

Van Albada, M. P. and Lagendijk, A.: Observation of weak localization of light in a random medium, Physical Review Letters, 55, 2692–2695, https://doi.org/10.1103/PhysRevLett.55.2692, 1985.

Van Albada, M. P., Van Der Mark, M. B., and Lagendijk, A.: Polarisation effects in weak localisation of light, Journal of Physics D: Applied Physics, 21, S28–S31, https://doi.org/10.1088/0022-3727/21/10S/009, 1988.

685   Van Albada, M. P., Van der Mark, M. B., and Lagendijk, A.: Experiments on weak localization of light and their interpretation, in: Scattering and Localization of Classical Waves in Random Media, pp. 97–136, World Scientific, 1990.

Van Der Mark, M. B., van Albada, M. P., and Lagendijk, A.: Light scattering in strongly scattering media: multiple scattering and weak localization, Physical Review B, 37, 3575, 1988.

Virtanen, P., Gommers, R., Oliphant, T. E., Haberland, M., Reddy, T., Cournapeau, D., Burovski, E., Peterson, P., Weckesser, W., Bright, J., van der Walt, S. J., Brett, M., Wilson, J., Millman, K. J., Mayorov, N., Nelson, A. R. J., Jones, E., Kern, R., Larson, E., Carey, C. J., Polat, İ., Feng, Y., Moore, E. W., VanderPlas, J., Laxalde, D., Perktold, J., Cimrman, R., Henriksen, I., Quintero, E. A., Harris, C. R., Archibald, A. M., Ribeiro, A. H., Pedregosa, F., van Mulbregt, P., and SciPy 1.0 Contributors: SciPy 1.0: Fundamental Algorithms for Scientific Computing in Python, Nature Methods, 17, 261–272, https://doi.org/10.1038/s41592-019-0686-2, 2020.

Wang, S., Feng, W., Kikuta, K., Chernyak, G., and Sato, M.: Ground-Based Bistatic Polarimetric Interferometric Synthetic Aperture Radar System, in: IGARSS 2019-2019 IEEE International Geoscience and Remote Sensing Symposium, pp. 8558–8561, IEEE, 2019.

Warren, S. G. and Brandt, R. E.: Optical constants of ice from the ultraviolet to the microwave: A revised compilation, Journal of Geophysical Research: Atmospheres, 113, 1–10, https://doi.org/10.1029/2007JD009744, 2008.

Wiesmann, A. and Werner, C.: SnowScat, X- to Ku-Band Scatterometer Development: D13 SnowScat User Manual, Tech. Rep. ESTEC/AO1-5311/06/NL/EL, ESA ESTEC / GAMMA, available from GAMMA Remote Sensing on request, 2010.

Wiesmann, A., Werner, C., Strozzi, T., Matzler, C., Nagler, T., Rott, H., Schneebeli, M., and Wegmuller, U.: SnowScat, X-to Ku-band scatterometer development, in: ESA Living Planet Symposium, vol. 686, p. 160, 2010.

Wolf, P., Maret, G., Akkermans, E., and Maynard, R.: Optical coherent backscattering by random media : an experimental study, Journal de Physique, 49, 63–75, https://doi.org/10.1051/jphys:0198800490106300, 1988.

Wolf, P. E. and Maret, G.: Weak localization and coherent backscattering of photons in disordered media, Physical Review Letters, 55, 2696–2699, https://doi.org/10.1103/PhysRevLett.55.2696, 1985.

Yushkova, O. V., Gavrik, A. L., Marchuk, V. N., Yushkov, V. V., Smirnov, V. M., Laptev, M. A., Chernyshev, B. V., Dutyshev, I. N., Lebedev, V. P., Medvedev, A. V., and Petrukovich, A. A.: Bistatic Radar Detection in the Luna-Resurs Mission, Solar System Research, 52, 287–300, https://doi.org/10.1134/S0038094618040081, 2018.

Zemp, M., Hoelzle, M., and Haeberli, W.: Distributed modelling of the regional climatic equilibrium line altitude of glaciers in the European Alps, Global and Planetary Change, 56, 83–100, https://doi.org/https://doi.org/10.1016/j.gloplacha.2006.07.002, climate Change Impacts on Mountain Glaciers and Permafrost, 2007.